GEOPHYSICS, VOL. 81, NO. 5 (SEPTEMBER-OCTOBER 2016); P. T233–T249, 15 FIGS., 5 TABLES.
10.1190/GEO2015-0660.1

Two efficient modeling schemes for fractional Laplacian viscoacoustic wave equation

Hanming Chen[1], Hui Zhou[1], Qingqing Li[1], and Yufeng Wang[1]

ABSTRACT

Recently, a decoupled fractional Laplacian viscoacoustic wave equation has been developed based on the constant-Q model to describe wave propagation in heterogeneous media. We have developed two efficient modeling schemes to solve the decoupled fractional Laplacian viscoacoustic wave equation. Both schemes can cope with spatial variable-order fractional Laplacians conveniently, and thus are applicable for modeling viscoacoustic wave propagation in heterogeneous media. Both schemes are based on fast Fourier transform, and have a spectral accuracy in space. The first scheme solves a modified wave equation with constant-order fractional Laplacians instead of spatial variable-order fractional Laplacians. Due to separate discretization of space and time, the first scheme has only first-order accuracy in time. Differently, the second scheme is based on an analytical wave propagator, and has a higher accuracy in time. To increase computational efficiency of the second modeling scheme, we have adopted the low-rank decomposition in heterogeneous media. We also evaluated the feasibility of applying an empirical approximation to approximate the fractional Laplacian that controls amplitude loss during wave propagation. When the empirical approximation is applied, our two modeling schemes become more efficient. With the help of numerical examples, we have verified the accuracy of our two modeling schemes with and without applying the empirical approximation, for a wide range of seismic quality factor (Q). We also compared computational efficiency of our two modeling schemes using numerical tests.

INTRODUCTION

The anelastic behavior of the earth can introduce strong attenuation and dispersion to propagating waves; thus, it is necessary to incorporate the viscous effects into seismic forward modeling and seismic data processing. In recent years, incorporation of attenuation into seismic imaging (Zhang et al., 2010; Dutta and Schuster, 2014; Sun et al., 2015) and inversion (Kurzmann et al., 2013; Bai et al., 2014; Chai et al., 2014, 2016) has become a common practice for exploration geophysicists. The constant-Q model (CQM; Kjartansson, 1979) provides an efficient parameterization of seismic attenuation in rocks, which motivates the development of constant-Q (CQ) or nearly constant-Q (NCQ) wave equations. Modeling CQM is easy in the frequency domain, and it can be realized by introducing a complex velocity (Aki and Richards, 1980). However, in the time domain, the relation between stress and strain is expressed by a temporal convolution operator, which requires a huge computational cost for numerical calculation. The attenuation model consisting of a series of standard linear solids (SLS) in parallel can closely approximate CQM over a specified frequency range, and this approach has been adopted by many researchers to develop time-domain viscoacoustic and viscoelastic wave equations (Day and Minster, 1984; Emmerich and Korn, 1987; Carcione et al., 1988a, 1988b; Blanch et al., 1995). Currently, these SLS-based NCQ wave equations have been used as forward engines in Q-compensated reverse time migration (RTM) and viscoacoustic full-waveform inversion (FWI) (Deng and McMechan, 2007; Bai et al., 2014). The SLS wave equation gains its popularity due to its flexibility in applying efficient finite-difference (FD) schemes for numerical calculation. However, to approximate the CQM with a desirable accuracy, one has to optimize the involved stress and strain relaxation times in advance (Blanch et al., 1995; Blanc et al., 2016). In addition, to model CQ attenuation and dispersion of seismic wave at long offsets, three SLS elements in parallel are usually

Manuscript received by the Editor 26 November 2015; revised manuscript received 17 May 2016; published online 3 August 2016.
[1]China University of Petroleum, State Key Laboratory of Petroleum Resources and Prospecting, CNPC Key Lab of Geophysical Exploration, Beijing, China. E-mail: huizhou@cup.edu.cn; huichanming@126.com; jyliqingqing@163.com; 13261295865@163.com.

required (Robertsson et al., 1994; Zhu et al., 2013), which increases the number of wave equations to be solved and the number of characterization parameters.

To develop more accurate NCQ wave equations, Carcione et al. (2002) introduce a temporal fractional derivative to describe Kjartansson's (1979) CQ stress-strain relation, and develop a simple CQ wave equation that only has two characterization parameters of velocity and seismic quality factor (Q). Mathematically, the discretization of temporal fractional derivative requires storing the whole time history of wavefield, which is unacceptable for practical numerical calculation. Later, Carcione (2010) transfers the fractional derivative from time to space by using the dispersion relation, and develops a fractional Laplacian wave equation that can be computed by fast Fourier transform (FFT) and inverse FFT (IFFT). Subsequently, Zhu and Harris (2014) develop a decoupled fractional Laplacian NCQ wave equation that includes two fractional Laplacians. The two fractional Laplacians have been proved to dominate dispersion and attenuation, respectively. The main contribution of Zhu and Harris's (2014) NCQ is splitting the fractional Laplacian that simultaneously controls dispersion and attenuation into two parts, one dominating dispersion and the other dominating attenuation. The decoupled effects are helpful for developing stable Q-compensated RTM (Zhu et al., 2014; Li et al., 2016). Meanwhile, Zhang et al. (2010) also develop a similar fractional Laplacian NCQ for Q-compensated RTM.

In the fractional Laplacian wave equation, the fractional orders are related to Q, and thus are spatially varying. Zhu and Harris (2014) simply adopt the average value of the spatially varying orders for numerical simulation. The average scheme is only reasonable for smoothly heterogeneous Q models, but is unsuitable for relatively sharp Q contrasts. The existing literatures have proposed three solutions to cope with the spatial variable-order fractional Laplacians. Li et al. (2014) use a weighted sum of two fixed-order fractional Laplacians to match the variable-order fractional Laplacian in the wavenumber domain, and estimate the weights using a least-squares (LS) approach. After the LS conduction, each spatial variable-order fractional Laplacian in the decoupled NCQ transforms into two fixed-order fractional Laplacians. That means that after the LS conduction, one needs to approximate four fractional Laplacians. From another point of view, the spatial variable-order fractional Laplacian represents a wavenumber-space mixed-domain matrix. Chen et al. (2014) adopt the low-rank decomposition (Fomel et al., 2013) to approximate each spatial variable-order fractional Laplacian in the decoupled NCQ. The LS and the low-rank schemes discretize time and space separately, and they have low-order accuracies in time. Almost at the same time, Sun et al. (2014, 2015) develop an efficient one-step low-rank modeling scheme to numerically solve the same decoupled fractional Laplacian NCQ. The spatially varying fractional orders of Laplacians are automatically handled in the low-rank decomposition. The one-step low-rank algorithm is based on an analytical time marching scheme, and has superior temporal accuracy and stability to the low-rank approximation scheme just for space as developed by Chen et al. (2014).

In this paper, we develop two efficient FFT-based modeling schemes for Zhu and Harris's (2014) decoupled NCQ. Both of our two schemes can efficiently cope with the spatial variable-order fractional Laplacians. Our first scheme adopts the weighted sum of two constant-order fractional Laplacians to approximate the spatial variable-order fractional Laplacian. However, different from the LS scheme developed by Li et al. (2014), the weights in our scheme are explicitly expressed instead of being implicitly determined by the LS approach. Our scheme should be more appealing for FWI, where explicit characterization parameters are preferred. Our second modeling scheme is based on an analytical wave propagator expressed in the wavenumber domain. When applied to simulate wave propagation in homogeneous media, the second modeling scheme is free of numerical dispersion and instability. When velocity and Q vary spatially, the wave propagator is viewed as a wavenumber-space mixed-domain matrix. We adopt the low-rank decomposition (Fomel et al., 2013) to approximate the mixed-domain propagator, and to further increase computational efficiency. Our low-rank modeling scheme is based on a three-step temporal extrapolation formula, and it is different from the one-step scheme developed by Sun et al. (2015). Effectiveness of our two modeling schemes will be demonstrated by using numerical examples. The accuracy and efficiency of our two modeling schemes will be compared as well.

METHOD

The decoupled fractional Laplacian NCQ wave equation (Zhu and Harris, 2014) is expressed by

$$\frac{1}{c^2}\frac{\partial^2 p}{\partial t^2} = \eta(-\nabla^2)^{\gamma+1}p + \tau\frac{\partial}{\partial t}(-\nabla^2)^{\gamma+\frac{1}{2}}p, \tag{1}$$

where

$$\eta = -c_o^{2\gamma}\omega_o^{-2\gamma}\cos(\pi\gamma), \quad \tau = -c_o^{2\gamma-1}\omega_o^{-2\gamma}\sin(\pi\gamma),$$
$$c = c_o\cos\left(\frac{\pi\gamma}{2}\right), \quad \gamma = \frac{1}{\pi}\arctan\left(\frac{1}{Q}\right), \tag{2}$$

where p represents the pressure, ∇^2 represents the Laplacian, and c_o denotes the wave velocity defined at a reference angular frequency ω_o. Accordingly, we define the reference frequency by $f_o = \omega_o/(2\pi)$. All the parameters of η, τ, γ, c_o, and Q in equation 2 are spatially dependent, denoted by $\mathbf{x}$, and vary spatially. Zhu and Harris (2014) replace the spatially varying order $\gamma(\mathbf{x})$ with the average value

$$\gamma_o = \frac{1}{N}\sum_{i=1}^{N}\gamma(x_i), \tag{3}$$

where x_i denotes the ith spatial grid node and N represents the total number of spatial grid nodes. We observe that $\eta(\mathbf{x})$ and $(-\nabla^2)^{\gamma(\mathbf{x})+1}$ affect the seismic wave phase, whereas $\tau(\mathbf{x})$ and $(-\nabla^2)^{\gamma(\mathbf{x})+1/2}$ affect the amplitude loss. The parameters $\eta(\mathbf{x})$ and $\tau(\mathbf{x})$ introduce a global effect to all frequency (or wavenumber) components. However, the fractional Laplacians produce different effects to different frequency components. The fractional Laplacians with the averaged γ_o in equation 3 cannot correctly describe dispersion and attenuation of different frequency components in heterogeneous media. Here, we present two effective schemes to cope with the spatial variable-order fractional Laplacians.

Temporal low-order modeling scheme

Assuming wave propagation in a homogeneous medium, we adopt the generalized Fourier pseudospectral method (Carcione, 2010) to define the wavenumber response of the fractional Laplacians, e.g.

$$(-\nabla^2)^{\gamma+1} p = F^{-1}\{|\mathbf{k}|^{2\gamma+2} F(p)\}, \tag{4}$$

where F and F^{-1} denote the forward and inverse Fourier transforms, respectively, and $|\mathbf{k}|$ represents the norm of the wavenumber vector $\mathbf{k}$. For brevity, we denote the norm as $k = |\mathbf{k}|$. Using the generalized Fourier pseudospectral method, we transform equation 1 into the wavenumber domain

$$\frac{1}{c^2\cos(\pi\gamma)}\frac{\partial^2 \tilde{p}}{\partial t^2} = -c_o^{2\gamma}\omega_o^{-2\gamma}k^{2\gamma+2}\tilde{p} - \frac{1}{Q}c_o^{2\gamma-1}\omega_o^{-2\gamma}k^{2\gamma+1}\frac{\partial \tilde{p}}{\partial t}, \tag{5}$$

where $\tilde{p}$ represents the wavefield in the wavenumber domain. An equivalent variation is applied to the first term on the right side of equation 5

$$c_o^{2\gamma}\omega_o^{-2\gamma}k^{2\gamma+2} = \lambda c_o^{2\gamma}\omega_d^{-2\gamma}k^{2\gamma+2} = \lambda k^2\left(\frac{k}{k_d}\right)^{2\gamma}, \tag{6}$$

where $\lambda = (\omega_d/\omega_o)^{2\gamma}$, $\omega_d = 2\pi f_d$ denotes the dominant angular frequency of the source, f_d denotes the dominant frequency, and $k_d = \omega_d/c_o$ represents the dominant wavenumber. If the reference velocity c_o is just defined at the dominant frequency f_d, one has $\lambda = 1$ and $f_o = f_d$.

With the condition of $2\gamma|\ln(k/k_d)| \ll 1$ satisfied, $(k/k_d)^{2\gamma}$ in equation 6 can be approximated by truncated Taylor-expansion (TE)

$$\left(\frac{k}{k_d}\right)^{2\gamma} \approx 1 + 2\gamma\ln\frac{k}{k_d}. \tag{7}$$

In general, for a low-loss medium ($Q \gg 1$), γ has a small value close to zero. One can prove $\gamma \approx 1/(\pi Q)$, so γ decreases as Q increases. On the other hand, for propagating waves excited by a band-limited source, most of the wave energy is distributed in a narrow wavenumber range around k_d. That means the condition $k/k_d \approx 1$ is approximately satisfied for most wave components. The two conditions of $\gamma \approx 0$ and $k/k_d \approx 1$ ensure the approximation accuracy in equation 7.

Then, we apply the TE approximation in equation 7 again

$$\begin{aligned} 1 + 2\gamma\ln\frac{k}{k_d} &= 1 + \frac{2\gamma}{\varepsilon}\ln\left(\frac{k}{k_d}\right)^{\varepsilon} \\ &= 1 + \frac{2\gamma}{\varepsilon}\ln\left(1 + \left(\frac{k}{k_d}\right)^{\varepsilon} - 1\right), \\ &\approx 1 + \frac{2\gamma}{\varepsilon}\left(\left(\frac{k}{k_d}\right)^{\varepsilon} - 1\right) \\ &= \left(1 - \frac{2\gamma}{\varepsilon}\right) + \frac{2\gamma}{\varepsilon}\frac{1}{k_d^{\varepsilon}}k^{\varepsilon}, \end{aligned} \tag{8}$$

where the parameter ε is introduced to guarantee $(k/k_d)^{\varepsilon} - 1$ sufficiently close to zero, or $(k/k_d)^{\varepsilon}$ close to one, which is the requirement of the truncated TE approximation applied in equation 8. Substitution of equation 8 into equation 7 and further into equation 6 leads to

$$c_o^{2\gamma}\omega_o^{-2\gamma}k^{2\gamma+2} \approx \lambda\left\{\left(1 - \frac{2\gamma}{\varepsilon}\right)k^2 + \frac{2\gamma}{\varepsilon}\frac{1}{k_d^{\varepsilon}}k^{2+\varepsilon}\right\}, \tag{9}$$

or equivalently ($k \neq 0$)

$$c_o^{2\gamma}\omega_o^{-2\gamma}k^{2\gamma} \approx \lambda\left\{\left(1 - \frac{2\gamma}{\varepsilon}\right) + \frac{2\gamma}{\varepsilon}\frac{1}{k_d^{\varepsilon}}k^{\varepsilon}\right\}. \tag{10}$$

To ensure the accuracy at high-wavenumber part, i.e., the part with $k > k_d$, one should choose $\varepsilon < 1$. To observe the effect of ε on the approximation accuracy in equation 10, we conduct a numerical test by using a homogeneous medium with $c_o = 4000$ m/s. The model is discretized into 400×400 nodes with a grid spacing of 20 m. For simplicity, we assume $\lambda = 1$, which means $\omega_o = \omega_d$ in equation 10. A series of Q and f_o are used to test the approximation accuracy in equation 10. We have observed that for each pair of Q and f_o, an optimal ε exists and minimizes the total relative errors expressed by

$$E_T = \sum_k \frac{|G_e(k) - G_a(k)|}{|G_e(k)|}, \tag{11}$$

where $G_e(k)$ represents the exact operator on the left side of equation 10 and $G_a(k)$ denotes the approximate operator on the right side of equation 10.

For each pair of Q and f_o, we gradually increase $1/\varepsilon$ from one to a large number with the increment of one. We observe that the value of E_T decreases first and then increases with the increase of $1/\varepsilon$. In addition, we find the optimal $1/\varepsilon$ corresponding to the minimum of E_T. In Table 1, we list the optimal $1/\varepsilon$ for a range of Q from 5 to 100, and a range of f_o from 5 to 50 Hz. One can find that the optimal $1/\varepsilon$ is proportional to Q, and independent of f_o. To demonstrate the magnitude of the approximation errors with the optimal $1/\varepsilon$, we list the maximum relative error for each pair of Q and f_o in Table 2. The maximum relative error is defined by

Table 1. Optimal $1/\varepsilon$ for different Q and frequencies.

Q	Frequency f_o (Hz)								
	5	10	15	20	25	30	35	40	50
5	8	8	8	8	8	8	8	8	8
10	16	16	16	16	16	16	16	16	16
20	31	31	31	31	31	31	31	31	31
50	79	79	79	79	79	79	79	79	79
100	157	157	157	157	157	157	157	157	157

$$E_M = \max\left\{\frac{|G_e(k) - G_a(k)|}{|G_e(k)|}\right\}. \quad (12)$$

Table 2 indicates that the relative error of the approximation in equation 10 has a small magnitude. The largest relative error in Table 2 is 0.387%, and appears when $Q = 5$ and $f_o = 50$ Hz. The value of E_M decreases as Q grows, however, slightly goes up as the frequency increases. Table 2 verifies that the approximation in equation 10 has a high accuracy for a wide range of Q and f_o. When Q becomes larger, E_M and E_T decrease further. The wide range of dominant frequencies from 5 to 50 Hz satisfies the requirements of most seismic applications.

However, our purpose is to adopt a uniform ε for all distinct Q values in heterogeneous media, instead of applying different ε for distinct Q. That requires a strong robustness of our approximation in equation 10. Figure 1 displays the relative errors of the approximation for $Q = 5$, 10, 20, 50, and 100 with the same $\varepsilon = 1/16$. For each Q, the errors for $f_o = 5$, 30, and 50 Hz are observed, respectively. Figure 1a shows a large relative error for $Q = 5$. However, when Q increases to 10, the error decreases to a low level as shown in Figure 1b because $\varepsilon = 1/16$ is optimal for $Q = 10$ as listed in Table 1. Figure 1c displays the relative errors for $Q = 20$, which reveals a visible error increase compared with Figure 1b. However, the maximum relative error is not beyond 1.0%. When Q further increases to 50 and 100, the relative errors become smaller, as displayed in Figure 1d and 1e.

We should point out that $\lambda = 1$ is not an essential condition for our approximation in equation 10. One can define c_o at an arbitrary reference frequency f_o. We assume $\lambda = 1$ only for simplicity, and f_o in Tables 1 and 2 and Figure 1 actually represents the dominant frequency f_d of the source. If $f_o \neq f_d$, the results in Tables 1 and 2 and in Figure 1 are still the same. Figure 1 indicates that the approximation with $\varepsilon = 1/16$ in equation 10 introduces a small error for $Q \geq 10$. We will further confirm the approximation accuracy with $\varepsilon = 1/16$ in the following sections.

The approximation in equation 10 can also be applied to the second term on the right side of equation 5

$$\frac{1}{Q}c_o^{2\gamma-1}\omega_o^{-2\gamma}k^{2\gamma+1} = \frac{\lambda}{Qc_o}k\left(\frac{k}{k_d}\right)^{2\gamma} \approx \frac{\lambda}{Qc_o}\left\{\left(1-\frac{2\gamma}{\varepsilon}\right)k + \frac{2\gamma}{\varepsilon}\frac{1}{k_d^{\varepsilon}}k^{1+\varepsilon}\right\}. \quad (13)$$

Substitution of equations 9 and 13 into equation 5 results in

$$\frac{1}{\lambda c^2\cos(\pi\gamma)}\frac{\partial^2\tilde{p}}{\partial t^2} = -\left\{\left[\left(1-\frac{2\gamma}{\varepsilon}\right)k^2 + \frac{2\gamma}{\varepsilon}\frac{1}{k_d^{\varepsilon}}k^{2+\varepsilon}\right]\tilde{p} + \frac{1}{Qc_o}\frac{\partial}{\partial t}\left[\left(1-\frac{2\gamma}{\varepsilon}\right)k + \frac{2\gamma}{\varepsilon}\frac{1}{k_d^{\varepsilon}}k^{1+\varepsilon}\right]\tilde{p}\right\}, \quad (14)$$

where $\gamma \approx 1/(\pi Q)$. By transforming equation 14 back to the space domain, we have

$$\frac{1}{\lambda c^2\cos(\pi\gamma)}\frac{\partial^2 p}{\partial t^2} = \left(1-\frac{2}{\varepsilon\pi Q}\right)\nabla^2 p - \frac{2}{\varepsilon\pi Q}\left(\frac{c_o}{\omega_d}\right)^{\varepsilon}(-\nabla^2)^{1+0.5\varepsilon}p - \frac{1}{Qc_o}\frac{\partial}{\partial t}\left\{\left(1-\frac{2}{\varepsilon\pi Q}\right)(-\nabla^2)^{0.5} + \frac{2}{\varepsilon\pi Q}\left(\frac{c_o}{\omega_d}\right)^{\varepsilon}(-\nabla^2)^{0.5+0.5\varepsilon}\right\}p. \quad (15)$$

Different from the original wave equation 1, the fractional orders in equation 15 are independent of the spatially varying Q. When ε is determined as a constant value, equation 15 only contains spatially constant-order fractional Laplacians, which facilitates numerical implementation. The fractional Laplacians in equation 15 are calculated by FFT to avoid spatial dispersion, as expressed in equation 4. The second-order temporal derivative in equation 15 is approximated by the second-order centered-grid FD operator, and the first-order temporal derivative is discretized by the backward FD operator. The temporal FD discretization leads to the global first-order accuracy in time.

Accuracy of equation 15 over long distance propagation

To verify the accuracy of equation 15, we compare the numerical solutions of equation 15 with those of the original wave equation 1. The numerical solution of equation 1 is regarded as a reference. We use a homogeneous medium with $c_o = 4000$ m/s. The medium is discretized into 761×761 nodes with a grid spacing of 20 m. We assume c_o is defined at the dominant frequency of the source, i.e., $\lambda = 1$ in equation 15. A time step of $\Delta t = 1$ ms is applied for 2.0 s simulation. We adopt the Ricker wavelets with $f_d = 5$, 30, and 50 Hz, respectively, as the excitation sources at the center of the medium. The solutions at a long distance of 5 km from the source

Table 2. The maximum relative error E_M (%) with the optimal $1/\varepsilon$ in Table 1.

Q	Frequency f_o (Hz)								
	5	10	15	20	25	30	35	40	50
5	1.44×10^{-1}	1.52×10^{-1}	1.99×10^{-1}	2.38×10^{-1}	2.70×10^{-1}	2.98×10^{-1}	3.24×10^{-1}	3.46×10^{-1}	3.87×10^{-1}
10	3.85×10^{-2}	3.54×10^{-2}	4.61×10^{-2}	5.46×10^{-2}	6.17×10^{-2}	6.79×10^{-2}	7.33×10^{-2}	7.82×10^{-2}	8.69×10^{-2}
20	7.30×10^{-3}	6.30×10^{-3}	8.20×10^{-3}	9.60×10^{-3}	1.08×10^{-2}	1.19×10^{-2}	1.28×10^{-2}	1.37×10^{-2}	1.51×10^{-2}
50	5.20×10^{-4}	4.30×10^{-4}	5.50×10^{-4}	6.50×10^{-4}	7.30×10^{-4}	8.10×10^{-4}	8.70×10^{-4}	9.20×10^{-4}	1.00×10^{-3}
100	1.14×10^{-5}	9.30×10^{-6}	1.20×10^{-5}	1.40×10^{-5}	1.60×10^{-5}	1.70×10^{-5}	1.90×10^{-5}	2.00×10^{-5}	1.20×10^{-5}

are compared. Figure 2 displays the solution comparison for $Q = 5$, 10, 20, 50, and 100, respectively. Each subplot of Figure 2 contains six panels. The upper three panels display the references and the numerical solutions of equation 15 with $\varepsilon = 1/8$ for $f_d = 5$, 30, and 50 Hz, respectively, whereas the lower three panels show the references and the numerical solutions of equation 15 with $\varepsilon = 1/16$ for the same three frequencies. We evaluate the match degree between the numerical solutions and the references using the root-mean-square (rms) error, which is marked in each panel.

Figure 2a indicates that for $Q = 5$, the numerical solutions of equation 15 with $\varepsilon = 1/8$ match the references much better than those computed with $\varepsilon = 1/16$. However, for $Q \geq 10$, especially for $Q = 10$ and 20, the numerical solutions with $\varepsilon = 1/8$ have larger rms errors than those computed with $\varepsilon = 1/16$, as displayed in Figure 2b–2e. The numerical solution with $\varepsilon = 1/16$ for $Q = 10$ exhibits a very small rms error because $\varepsilon = 1/16$ is optimal for $Q = 10$ (see Table 1). For $Q = 20$, the rms errors of the solutions with $\varepsilon = 1/16$ become much larger than those for $Q = 10$. However, under such an rms error level (2.20×10^{-3} when $f_d = 50$ Hz), the numerical solutions with $\varepsilon = 1/16$ still agree with the references very well, as shown in Figure 2c. When Q further increases to 50 and 100 (Figure 2d and 2e), the rms errors decrease. We have tested larger Q, and observed that the rms error decreases with the increase of Q. Note that some severe waveform distortions appear in the numerical solutions in Figure 2d and 2e. They are the results of temporal dispersion.

The numerical solution comparison in Figure 2 verifies that our wave equation 15 with $\varepsilon = 1/16$ can simulate almost the same wavefield as the original wave equation 1 for $Q \geq 10$ at a long distance. When a relatively low-frequency source is applied, our wave equation 15 with $\varepsilon = 1/16$ exhibits a high accuracy as well, even for a rather small value of $Q = 5$, as demonstrated in Figure 2a. Therefore, we suggest using $\varepsilon = 1/16$ in equation 15. In the following sections, we set $\varepsilon = 1/16$ in equation 15. Numerical simulation of equation 15 is referred to as our first modeling scheme.

Low-rank modeling scheme

Our second modeling scheme starts from equation 5, which represents a second-order linear differential equation with respect to time. It has an analytical solution (Arfken et al., 2013)

$$\tilde{p}(t) = e^{\alpha t}\{A\cos(\beta t) + B\sin(\beta t)\}, \tag{16}$$

where A and B are two undetermined coefficients, and

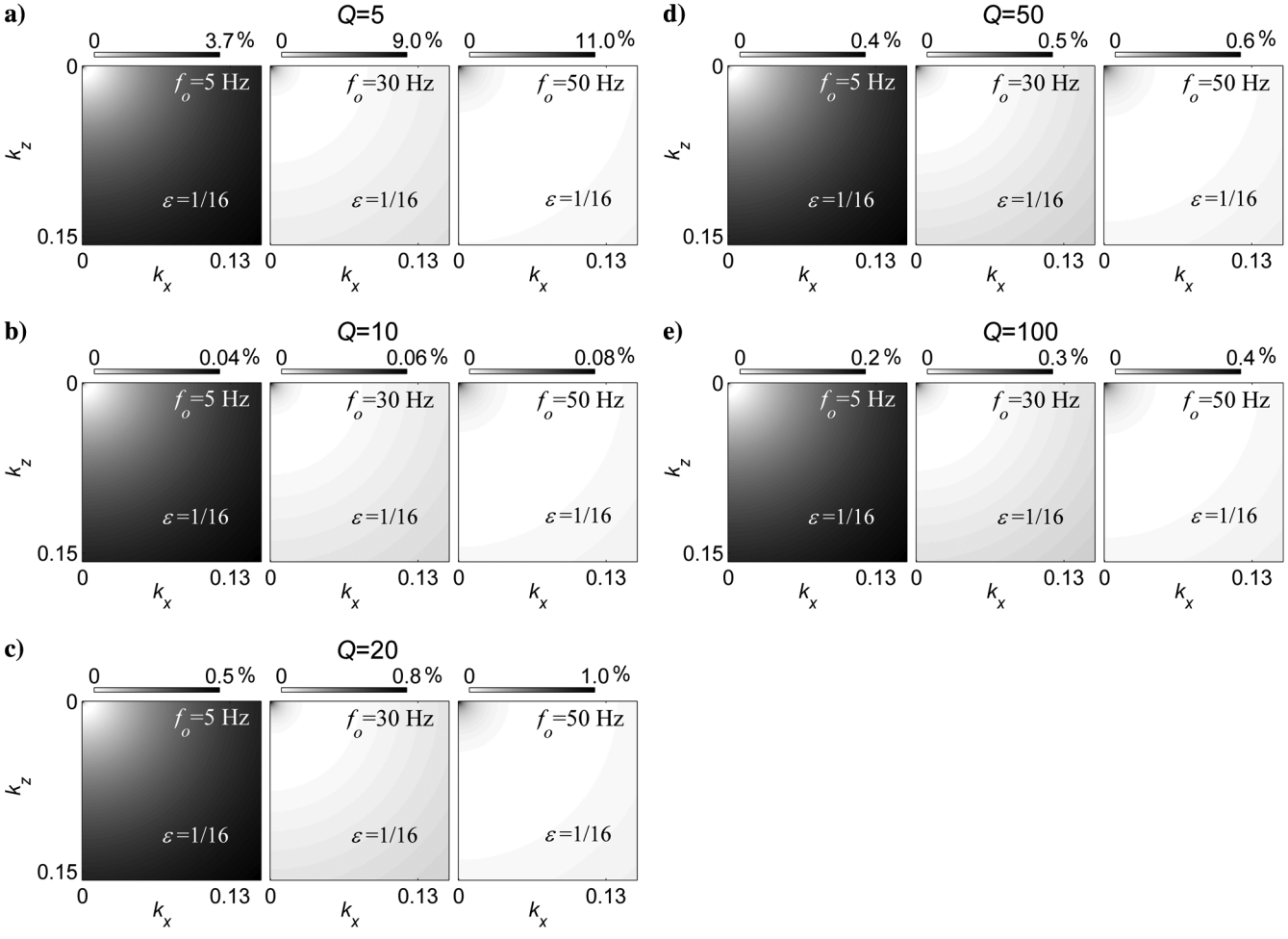

Figure 1. Relative errors of the approximation in equation 10 for (a) $Q = 5$, (b) 10, (c) 20, (d) 50, and (e) 100 with $\varepsilon = 1/16$. In each subplot, the left, middle, and right panels display errors for $f_o = 5$, 30, and 50 Hz, respectively. The symbols k_x and k_z denote x- and z-axial wavenumbers accordingly.

$$\alpha = -\frac{1}{2}c_o^{2\gamma+1}\omega_o^{-2\gamma}\cos^2\left(\frac{\pi\gamma}{2}\right)\sin(\pi\gamma)k^{2\gamma+1},$$
$$\beta = \frac{1}{2}c_o^{\gamma+1}\omega_o^{-\gamma}\cos\left(\frac{\pi\gamma}{2}\right)\left\{4\cos(\pi\gamma) - \cos^2\left(\frac{\pi\gamma}{2}\right)\sin^2(\pi\gamma)\right\}^{\frac{1}{2}}k^{\gamma+1}. \quad (17)$$

Based on equation 16, one can obtain an analytical three-step time marching scheme

$$\tilde{p}(t+\Delta t) = 2e^{\alpha\Delta t}\cos(\beta\Delta t)\tilde{p}(t) - e^{2\alpha\Delta t}\tilde{p}(t-\Delta t). \quad (18)$$

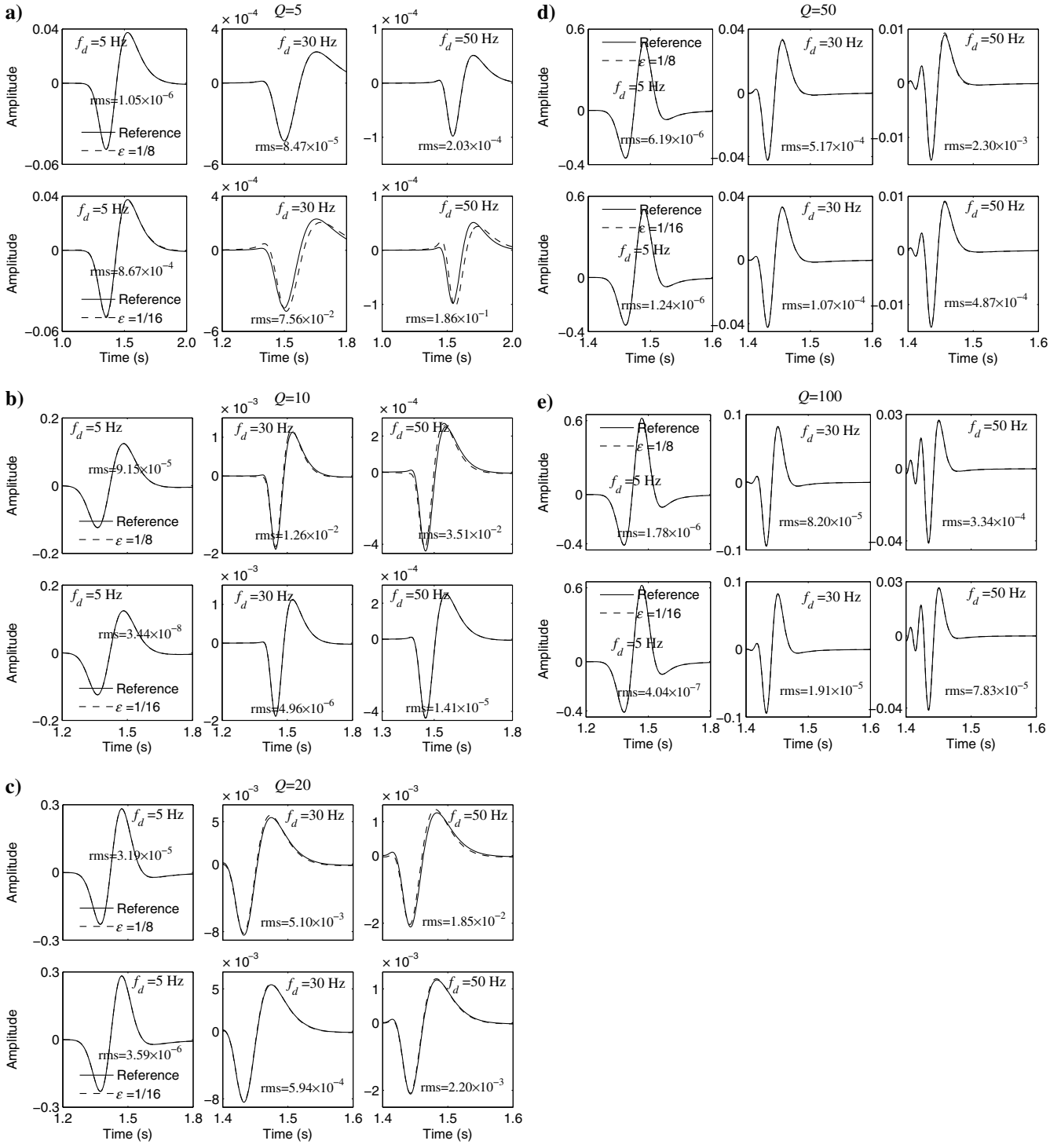

Figure 2. Comparison of numerical solutions between equations 1 (reference) and 15 for (a) $Q = 5$, (b) 10, (c) 20, (d) 50, and (e) 100. In each subplot, the upper three panels show solutions of equation 15 with $\varepsilon = 1/8$ for $f_d = 5$, 30, and 50 Hz, respectively, and the lower three panels show solutions with $\varepsilon = 1/16$ for the same three frequencies.

The derivation for equations 16–18 is described in Appendix A. Because equation 18 is based on the analytical solution, the time marching scheme is free of instability and numerical dispersion. Considering Δt is small, we apply the TE approximation

$$e^{\alpha\Delta t} \approx 1 + \alpha\Delta t, e^{2\alpha\Delta t} \approx 1 + 2\alpha\Delta t, \tag{19}$$

in equation 18 and reformulate it as

$$\frac{\tilde{p}(t+\Delta t) + \tilde{p}(t-\Delta t) - 2\tilde{p}(t)}{(\bar{\eta}\Delta t)^2} = L_{\alpha,\beta}\tilde{p}(t) + \frac{\bar{\tau}}{\bar{\eta}^2\Delta t}k^{2\gamma+1}\{\tilde{p}(t) - \tilde{p}(t-\Delta t)\}, \tag{20}$$

where

$$L_{\alpha,\beta} = \frac{2\{\cos(\beta\Delta t) - 1\}(1 + \alpha\Delta t)}{(\bar{\eta}\Delta t)^2}, \tag{21}$$

and

$$\bar{\eta} = \frac{1}{2}c_o^{\gamma+1}\omega_o^{-\gamma}\cos\left(\frac{\pi\gamma}{2}\right)\left\{4\cos(\pi\gamma) - \cos^2\left(\frac{\pi\gamma}{2}\right)\sin^2(\pi\gamma)\right\}^{\frac{1}{2}},$$
$$\bar{\tau} = -c_o^{2\gamma+1}\omega_o^{-2\gamma}\cos^2\left(\frac{\pi\gamma}{2}\right)\sin(\pi\gamma) \approx -\frac{1}{Q}c_o^{2\gamma+1}\omega_o^{-2\gamma}. \tag{22}$$

The parameters $\bar{\eta}$ and $\bar{\tau}$ can be explicitly expressed by c_o and Q, and the derivation is provided in Appendix B.

Equation 20 can be regarded as the discretization of the following wave equation in the time and space domain:

$$\frac{\partial^2 p}{\partial t^2} = \bar{\eta}^2\hat{\nabla}^2 p + \bar{\tau}\frac{\partial}{\partial t}(-\nabla^2)^{\gamma+\frac{1}{2}}p, \tag{23}$$

where $\hat{\nabla}^2$ represents a pseudo-Laplacian with the wavenumber response defined in equation 21. When Q approaches infinity, the wavenumber response degrades to that of the acoustic pseudo-Laplacian, as developed by Fomel et al. (2013). The modified wavenumber response can compensate spatial and temporal dispersion due to discretization.

To further simplify equation 23, we apply the TE approximation in equation 13 to the wavenumber response of $\bar{\tau}(-\nabla^2)^{\gamma+1/2}$ in the wavenumber domain

$$\bar{\tau}k^{2\gamma+1} = -\frac{1}{Q}c_o^{2\gamma+1}\omega_o^{-2\gamma}k^{2\gamma+1} = -\frac{\lambda c_o}{Q}k\left(\frac{k}{k_d}\right)^{2\gamma} \approx -\frac{\lambda c_o}{Q}\left\{\left(1 - \frac{2\gamma}{\varepsilon}\right)k + \frac{2\gamma}{\varepsilon}\frac{1}{k_d^{\varepsilon}}k^{1+\varepsilon}\right\}, \tag{24}$$

where $\varepsilon = 1/16$. By transforming equation 24 back to the space domain and inserting it into equation 23, we obtain

$$\frac{\partial^2 p}{\partial t^2} = \bar{\eta}^2\hat{\nabla}^2 p - \frac{\lambda c_o}{Q}\frac{\partial}{\partial t}\left\{\left(1 - \frac{2}{\varepsilon\pi Q}\right)(-\nabla^2)^{0.5} + \frac{2}{\varepsilon\pi Q}\left(\frac{c_o}{\omega_d}\right)^{\varepsilon}(-\nabla^2)^{0.5+0.5\varepsilon}\right\}p. \tag{25}$$

The pseudo-Laplacian and fractional Laplacians are calculated with the help of FFT, and the temporal derivatives are discretized by the FD operators, as expressed in equation 20. The key to attain stable temporal extrapolation is applying the modified wavenumber response (equation 21) for the pseudo-Laplacian in equation 25. Numerical simulation of equation 25 is referred to as our second modeling scheme.

Accuracy of equation 25 over long distance propagation

We adopt the TE approximations in equations 19 and 24 to derive equation 25, and the approximations would introduce errors to the analytical time marching scheme in equation 18. To investigate the accuracy, we repeat the numerical solution comparison at a long distance of 5 km. Figure 3 displays the numerical solutions of the analytical time marching scheme in equation 18 (reference), and the numerical solutions of equation 25 for $Q = 5$ and 10, respectively. For each Q, the Ricker wavelets with three dominant frequencies of $f_d = 5$, 30, and 50 Hz are used as excitation sources separately. Figure 3a indicates that the numerical solutions of equation 25 for $Q = 5$ exhibit a slight phase-shift off the references. The phase shift causes a relatively large rms error of 9.30×10^{-3} when $f_d = 50$ Hz. However, when Q increases to 10, no visible phase shifts appear in the numerical solutions of equation 25, and the rms errors are smaller than 3.0×10^{-3}, as displayed in Figure 3b. We have tested the accuracy for larger Q, and found that the rms errors decrease with the increase of Q.

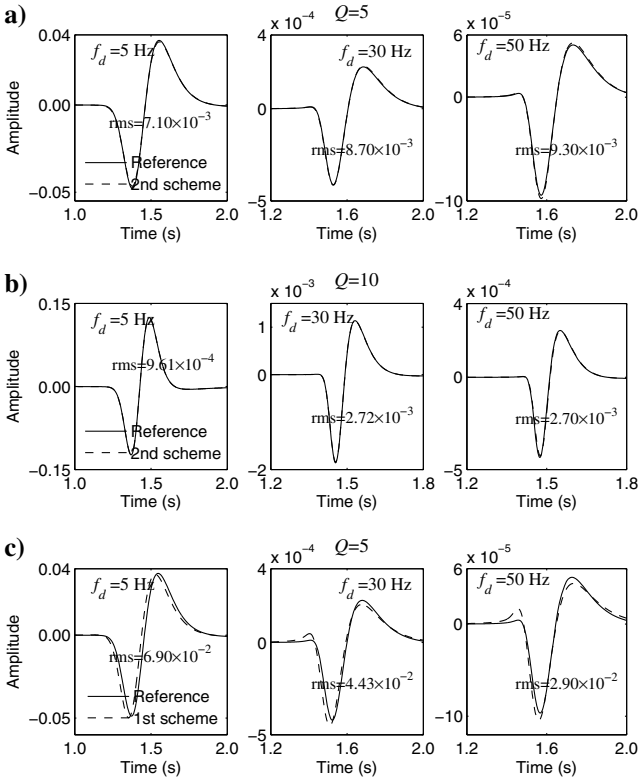

Figure 3. Comparison of numerical solutions between equations 18 (reference) and 25 for (a) $Q = 5$, (b) 10, and (c) comparison between equations 18 (reference) and 15 (first scheme) for $Q = 5$.

To compare the accuracies of our first and second modeling schemes for $Q = 5$, we contrast the numerical solutions of equation 15 to the references in Figure 3c. By comparing Figure 3c with Figure 3a, one can observe that our first modeling scheme introduces larger phase and amplitude misfits off the references, and naturally causes larger rms errors than our second scheme. The comparison indicates that our second modeling scheme has a higher accuracy than our first scheme for extremely small Q.

Another issue that needs to be addressed in our second modeling scheme is the numerical implementation of the pseudo-Laplacian in equation 25. In heterogeneous media, c_o and Q vary spatially and the operator in equation 21 represents a wavenumber-space mixed-domain matrix

$$\mathbf{L}_{\alpha,\beta}(\mathbf{x},|\mathbf{k}|) = \frac{2\{\cos(\beta(\mathbf{x},|\mathbf{k}|)\Delta t) - 1\}\{1 + \alpha(\mathbf{x},|\mathbf{k}|)\Delta t\}}{\{\bar{\eta}(\mathbf{x})\Delta t\}^2}. \tag{26}$$

When one applies the pseudo-Laplacian to p in the space domain, one equivalently conducts the calculation in the wavenumber domain

$$p(t,\mathbf{x}) = F^{-1}\{\mathbf{L}_{\alpha,\beta}(\mathbf{x},|\mathbf{k}|)\tilde{p}(t,|\mathbf{k}|)\}. \tag{27}$$

Theoretically, for each distinct value of c_o or Q, one needs to perform one time of IFFT for the calculation in equation 27. This method is referred to as the pointwise FFT scheme. The pointwise scheme is an effective numerical approach to handle the mixed-domain operator; however, its computational cost is unacceptable. To increase the computational efficiency, we adopt the low-rank decomposition (Fomel et al., 2013) to approximate the mixed-domain matrix

$$\mathbf{L}_{\alpha,\beta}(\mathbf{x},|\mathbf{k}|) \approx \mathbf{W}_1(\mathbf{x},|\mathbf{k}|_m)_{N\times m}\mathbf{G}_{m\times n}\mathbf{W}_2(\mathbf{x}_n,|\mathbf{k}|)_{n\times N}, \tag{28}$$

where m and n represent ranks of the decomposition, and they influence the decomposition accuracy, and N denotes the total grid number. For a detailed interpretation of the three matrices $\mathbf{W}_1$, $\mathbf{G}$, and $\mathbf{W}_2$ in equation 28, one can refer to Fomel et al. (2013). After the decomposition, we reformulate the calculation in equation 27 as

$$p(t,\mathbf{x}) \approx \sum_{i=1}^{m}\mathbf{W}_1(\mathbf{x},|\mathbf{k}|_i)\sum_{j=1}^{n} g_{i,j}F^{-1}\{\mathbf{W}_2(\mathbf{x}_j,|\mathbf{k}|)\tilde{p}(t,|\mathbf{k}|)\}, \tag{29}$$

where $g_{i,j}$ represents the ith row and jth column element of $\mathbf{G}$. By using equation 29, we require n times of IFFT to calculate the pseudo-Laplacian per time step. For heterogeneous media, n increases with the spatial complexity of the velocity and Q models, and usually ranges from 2 to 5. In total, to simulate equation 25, we need two times of FFT and $n + 2$ times of IFFT per time step.

To demonstrate the feasibility of the viscoacoustic low-rank decomposition in equation 28, we test the decomposition accuracy using a 2D model with the total grid number of $N = 128 \times 128$ (Figure 4) and the grid spacing of 10×10 m. The velocity linearly increases from 1500 to 4500 m/s along the depth. The Q model is generated by using an empirical formula. The minimum Q is 34 at the surface, and the maximum Q is 383 at the bottom. A time step of 1.5 ms is adopted to calculate the exact mixed-domain matrix $\mathbf{L}_{\alpha,\beta}(\mathbf{x},|\mathbf{k}|)$ in equation 26. Figure 5a displays the exact matrix, and Figure 5b and 5c displays the absolute errors of the low-rank decomposition with $m = n = 2$ and $m = n = 3$, respectively. One can observe that with a larger rank, the low-rank decomposition achieves a higher accuracy. For this pair of c_o and Q models, $m = n = 3$ is enough for controlling the decomposition error at a low level (smaller than 1×10^{-4}), as displayed in Figure 5c. A larger rank of m and n decreases decomposition error further, but leads to more times of IFFT during wave propagation.

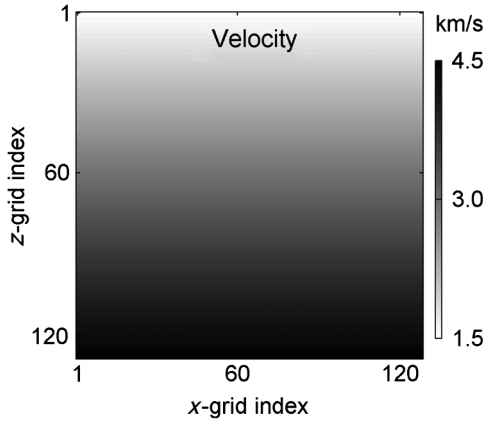

Figure 4. A 2D velocity model with a total grid number of 128×128.

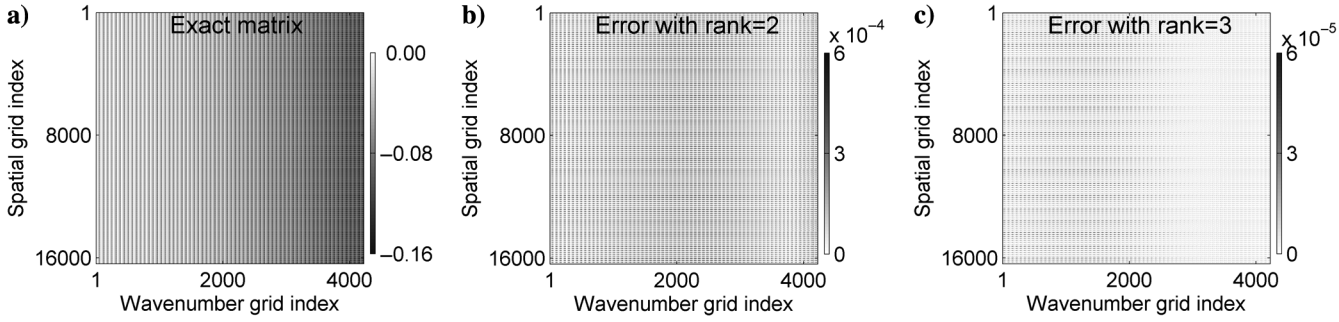

Figure 5. Illustration of viscoacoustic low-rank decomposition accuracy, (a) exact mixed-domain matrix, and low-rank decomposition absolute errors with the ranks of (b) $m = n = 2$ and (c) $m = n = 3$.

Efficiency comparison between our two modeling schemes

Our first modeling scheme simulates equation 15, and discretizes time and space separately, which leads to the first-order accuracy in time. The temporal low-order accuracy would introduce great temporal dispersion when a relatively high-frequency source is applied (see Figure 2d and 2e with $f_d = 30$, 50 Hz). To control numerical dispersion caused by temporal discretization, one has to adopt a tiny time step for temporal extrapolation, which increases the computational cost. Our second modeling scheme is derived from the analytical time marching scheme, and has a higher temporal accuracy. To compare computational efficiency of our two modeling schemes, we conduct numerical simulations using the same homogeneous medium and grid size as those used to obtain Figures 2 and 3. A Ricker wavelet with $f_d = 30$ Hz is applied as the source. We generate a reference solution at a distance of 5 km from the source by using the analytical time marching scheme in equation 18 with the time step of $\Delta t = 1$ ms. Then, we compute the numerical solutions at the same distance by using our two schemes, respectively. The rms errors of the numerical solutions of our two schemes are calculated to evaluate their match degrees with the reference. We use two relatively large values of $Q = 20$ and 100 for the numerical solution comparison.

Table 3 lists rms errors of the numerical solutions of our two schemes for $Q = 20$. The second scheme introduces a small rms error of 6.10×10^{-4} with $\Delta t = 1$ ms. In contrast, the first scheme causes a much larger rms error of 4.06×10^{-2} with the same time step. Even with the two times smaller time step of $\Delta t = 0.5$ ms, the first modeling still causes a larger error than our second modeling scheme. When the time step is further reduced to $\Delta t = 0.25$ ms, the first scheme achieves a slightly better accuracy than the second scheme with $\Delta t = 1$ ms. Table 4 lists the comparison for $Q = 100$. Compared with $Q = 20$, the second modeling scheme produces a smaller rms error of 5.76×10^{-6}. In contrast, the first modeling scheme causes a much larger rms error of 1.36×10^{-1} with $\Delta t = 1$ ms. When the time step is halved to 0.5 ms, the rms error decreases to a low level, but still much larger than that of the second scheme. When the time step is further halved to 0.25 ms, the rms error of the first scheme presents an increase. To verify the increase, we have repeated the comparison using the acoustic-wave equation, and observed a similar increase. Note that the rms errors of the numerical solutions of the second modeling scheme with $\Delta t = 1$ ms are already very small, and we have no need to use a smaller time step. Therefore, the rms errors of the second scheme with $\Delta t = 0.5, 0.25$ ms are not listed in Tables 3 and 4.

Tables 3 and 4 indicate that to attain a comparable accuracy, the first scheme has to use a smaller time step than the second scheme. For wave propagation in heterogeneous media, the low-rank decomposition in the second scheme would also introduce errors. The presented numerical examples by Fomel et al. (2013) and Song et al. (2013) indicate that the ranks of $m = n = 5$ are enough for ensuring a desirable simulation accuracy in moderately heterogeneous models, such as the BP model (Billette and Brandsberg-Dahl, 2014) with the maximum velocity contrast ratio of approximately 3.0, and the Marmousi model with the ratio of approximately 4.5. We perform a rather conservative comparison, in which the first modeling scheme adopts a two times smaller time step than our second modeling scheme. With the ranks of $m = n = 5$, the second modeling scheme requires two times of FFT and seven times of IFFT per time step (see equation 25). In

Table 3. The rms errors of numerical solutions of our two modeling schemes for $Q = 20$ and $f_d = 30$ Hz. The reference is computed by the analytical time marching scheme in equation 18 with $\Delta t = 1$ ms.

Δt (ms)	First scheme	Second scheme
1.0	4.06×10^{-2}	6.10×10^{-4}
0.5	1.30×10^{-3}	—
0.25	1.51×10^{-4}	—

Table 4. The rms errors of numerical solutions of our two modeling schemes for $Q = 100$ and $f_d = 30$ Hz. The reference is computed by the analytical time marching scheme in equation 18 with $\Delta t = 1$ ms.

Δt (ms)	First scheme	Second scheme
1.0	1.36×10^{-1}	5.76×10^{-6}
0.5	3.70×10^{-3}	—
0.25	5.20×10^{-3}	—

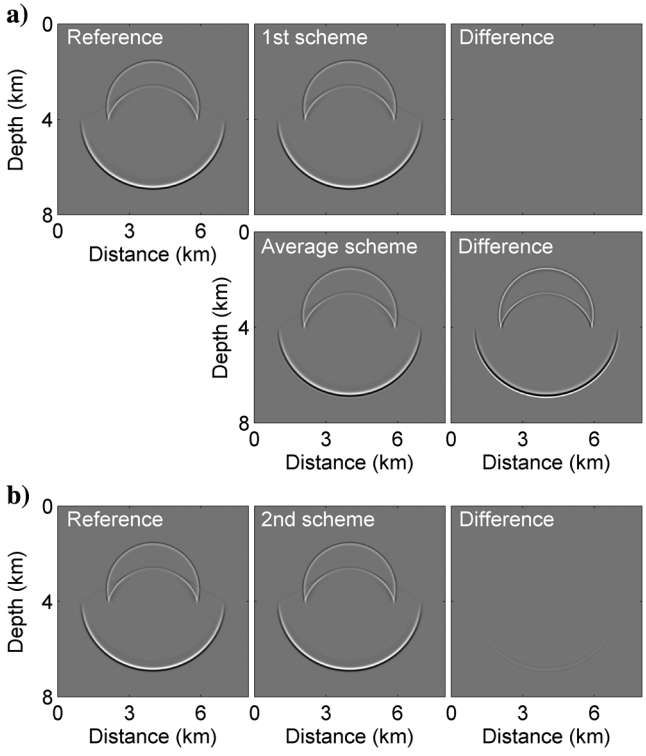

Figure 6. Snapshots at 1.0 s computed with $\Delta t = 1$ ms by (a) pointwise FFT scheme (reference), our first scheme, the average scheme, and snapshot differences from the reference, (b) the pointwise FFT scheme with $\Delta t = 0.25$ ms, our second scheme with $\Delta t = 1.0$ ms, and their differences.

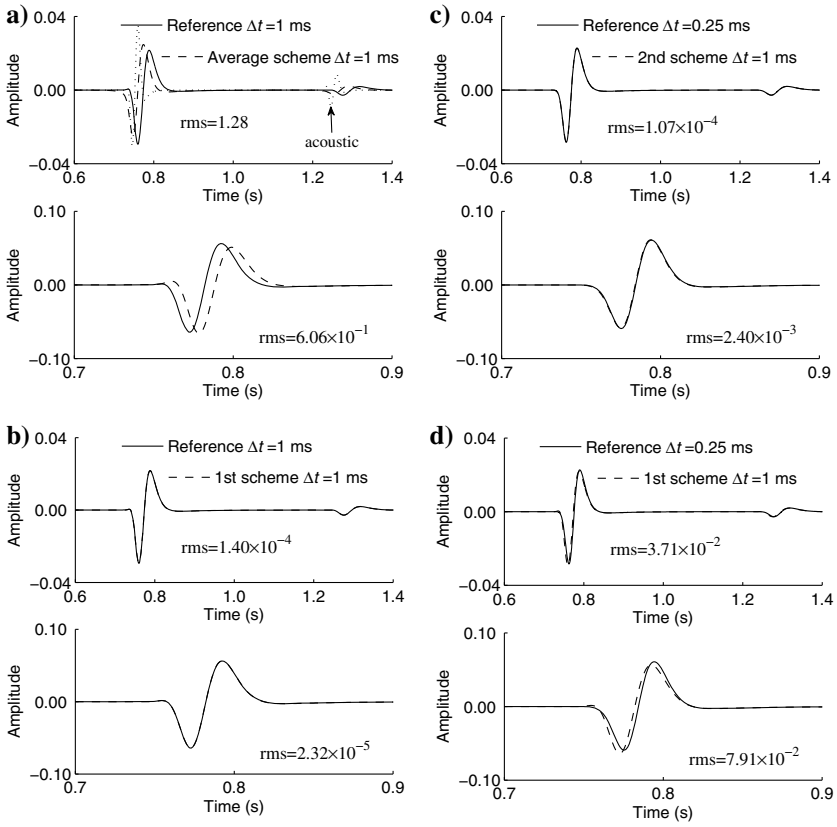

Figure 7. Seismograms comparison between (a) reference and those computed by the average scheme using $\Delta t = 1.0$ ms, (b) reference and our first scheme using $\Delta t = 1.0$ ms, (c) reference using $\Delta t = 0.25$ ms and our second scheme using $\Delta t = 1.0$ ms, (d) reference using $\Delta t = 0.25$ ms and our first scheme using $\Delta t = 1.0$ ms. In each subplot, the upper and lower panels show seismograms at (4,2) and (4,6)km, respectively. Note that the dotted line in the upper panel in Figure 7a denotes the acoustic trace with the amplitude multiplied by 0.1.

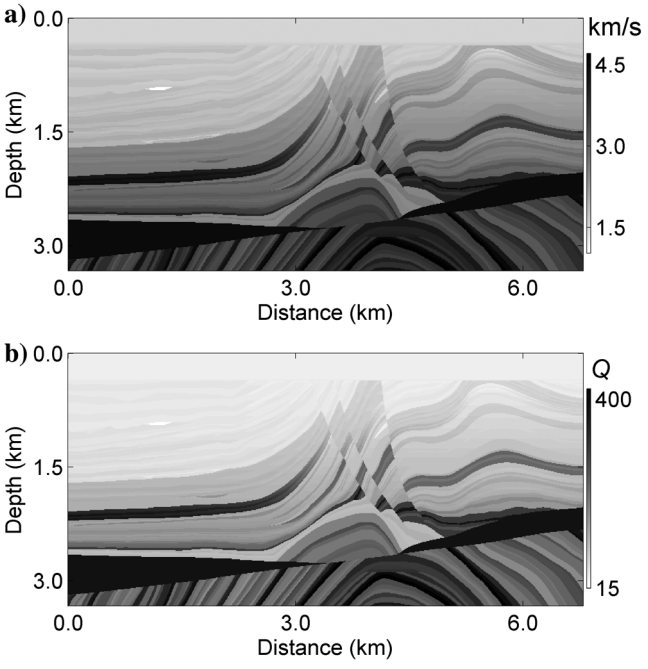

Figure 8. Marmousi model (a) c_o and (b) Q.

contrast, the first modeling scheme requires two times of FFT and four times of IFFT per time step (see equation 15). Therefore, the second scheme can achieve a theoretical speed-up factor of approximately 1.33 compared with the first modeling scheme. We point out that the low-rank decomposition in equation 28 and the low-rank calculation in equation 29 also require floating-point operations (FPOs), besides those involved in FFT and IFFT, which leads to a slight efficiency decrease of the second scheme. Fortunately, the low-rank decomposition is precomputation from a wave-propagation perspective.

NUMERICAL EXAMPLES

A simple two-layer model

We first demonstrate the accuracies of our two modeling schemes by simulating viscoacoustic wave propagation in a simple two-layer model with the size of 8×8 km. The model contains a horizontal interface at the depth of $z = 4.0$ km. The velocity and Q of the first layer are 2 km/s and 20, and those of the second layer are 4 km/s and 100. We adopt the grid spacing of 10×10 m to discretize the model, and a Ricker wavelet with $f_d = 30$ Hz to excite the wavefield at $(x, z) = (4.0, 3.5)$km. The velocity model c_o is defined at f_d, which means $\lambda = 1$ in equations 15 and 25. We adopt Zhu and Harris (2014) averaging scheme, our first and second modeling schemes to simulate wave propagation, respectively. To evaluate the accuracies of different schemes, we adopt the pointwise FFT scheme to simulate the original wave equation 1 to obtain a reference wavefield. The pointwise FFT scheme calculates the fractional Laplacians (see equation 4) for the upper and lower layers separately. Therefore, the pointwise FFT scheme is an effective approach to handle the spatial variable-order fractional Laplacians.

Figure 6a displays the snapshots at 1.0 s computed by the pointwise FFT scheme (reference), our first modeling scheme, and Zhu and Harris (2014) averaging scheme with the same time step of $\Delta t = 1$ ms. The snapshot differences from the reference are displayed as well. All the snapshots and the differences are shown in the same amplitude range. One can observe that the snapshot difference between our first scheme and the reference is almost zero, which proves the accuracy of our first scheme. However, compared with the reference snapshot, the snapshot computed by Zhu and Harris (2014) averaging scheme exhibits a visible difference, as displayed by the last panel in Figure 6a. We also demonstrate the accuracy of our second scheme by comparing its simulation result with that of the pointwise FFT scheme. Because the pointwise scheme only has the first-order temporal accuracy that is inconsistent with our second scheme, we adopt a tiny time step of $\Delta t = 0.25$ ms for the pointwise scheme, and a four times larger time step of $\Delta t = 1.0$ ms for our second scheme. Figure 6b displays the snapshot at 1.0 s computed by the pointwise scheme and our second scheme with the ranks of $m = n = 2$. The difference be-

tween them is minimal, as shown in the third panel in Figure 6b, which validates the accuracy of our second scheme.

For a detailed comparison, we display the seismograms recorded at $(x, z) = (4, 2)$ km and $(x, z) = (4, 6)$ km in Figure 7. The seismograms at the two positions are separately shown in the upper and lower panels in each subplot of Figure 7. The first position is located above the interface and source, so the seismograms consist of a direct-arrival and reflected waveform. The second position is located below the interface, and the seismograms only contain transmitted waveform. Figure 7a displays the seismograms computed by Zhu and Harris (2014) averaging scheme and by the pointwise FFT scheme with $\Delta t = 1$ ms. A large difference between the two seismograms can be observed in Figure 7a. Note that we also plot the acoustic trace in the upper panel in Figure 7a (see the dotted line) to demonstrate that attenuation physically delays the wave relative to nonattenuation (acoustic) case. The amplitude of the acoustic trace is multiplied by 0.1. One can observe from Figure 7b that the seismogram simulated by our first scheme fits the reference very well. The seismograms simulated by our second scheme with $\Delta t = 1$ ms also match the reference with $\Delta t = 0.25$ ms very well, as displayed in Figure 7c. However, one can observe from Figure 7d that the seismogram computed by our first scheme with $\Delta t = 1$ ms exhibit a visible misfit off the reference with $\Delta t = 0.25$ ms. The misfit is caused by the temporal dispersion.

We observe that a maximum time step of $\Delta t = 1.1$ ms can be used for the first scheme for stability; however, a maximum time step of approximately $\Delta t = 5.5$ ms corresponding to the Nyquist frequency can be applied to the second scheme. Therefore, to simulate wave propagation in such a simple two-layer model, the second scheme is more efficient than the first scheme because the second scheme enables a much larger time step.

Marmousi model

We further verify the accuracies of our two modeling schemes by simulating wave propagation in the Marmousi model (Figure 8). This model contains complex structures and has a maximum velocity contrast ratio of approximately 4.6. The model is discretized into 680×334 nodes with the grid spacing of 10 m. We adopt a Ricker wavelet excitation source with $f_d = 20$ Hz located at $(x, z) = (3.4, 0)$ km. We assume that the velocity in Figure 8 is defined at 20 Hz as well. Our two modeling schemes are applied to simulate wave propagation in the model, respectively. We have observed that a maximum time step of $\Delta t = 0.9$ ms can be applied to the first scheme to avoid numerical instability. However, the second scheme with the ranks larger than two enables a maximum time step of $\Delta t = 1.6$ ms. To facilitate the comparison between our two schemes, we use $\Delta t = 0.9$ ms for the first scheme and $\Delta t = 1.5$ ms for the second scheme. We run our CUDA C codes on a single GPU of NVIDIA GTX 760 to extrapolate wavefield to 4.5 s. Table 5 lists the elapsed CPU time of our two schemes. The ranks of four are applied in the second scheme. If one only considers the cost due to FFT and IFFT, the second scheme should achieve approximately 20% efficiency gain compared with the first scheme. However, the second scheme practically takes a little longer time than the first scheme, as listed in Table 5. This is caused by the extra FPOs involved in the low-rank decomposition in equation 28 and the summation operations in equation 29.

Table 5. Elapsed time of our first and second modeling schemes for simulating 4.5 s wave propagation. The ranks of $m = n = 4$ are adopted in the second scheme.

	Δt (ms)	Times of FFT and IFFT per step	Number of time steps for 4.5 s simulation	Elapsed time (s)
First scheme	0.9	6	5001	47.32
Second scheme	1.5	8	3001	48.16
First scheme	0.45	6	10,001	95.12

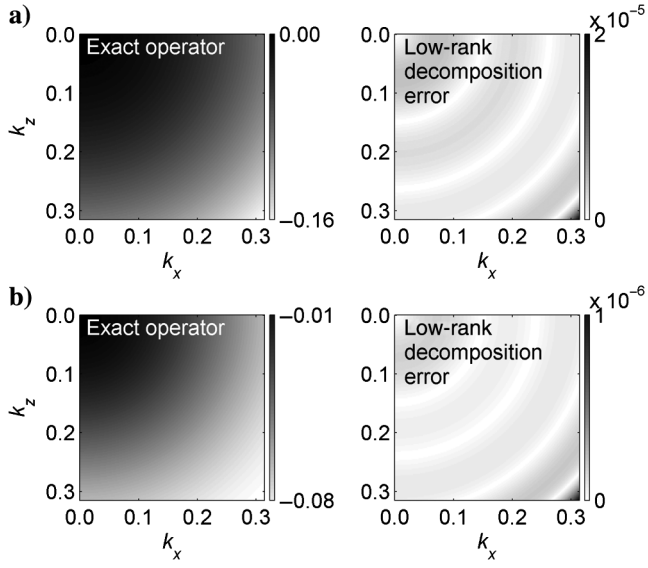

Figure 9. Observation of the low-rank decomposition accuracy at (a) $(x, z) = (990, 990)$ m with $c_o = 1849$ m/s, $Q = 54$ and (b) $(x, z) = (990, 2830)$ m with $c_o = 4500$ m/s, $Q = 383$.

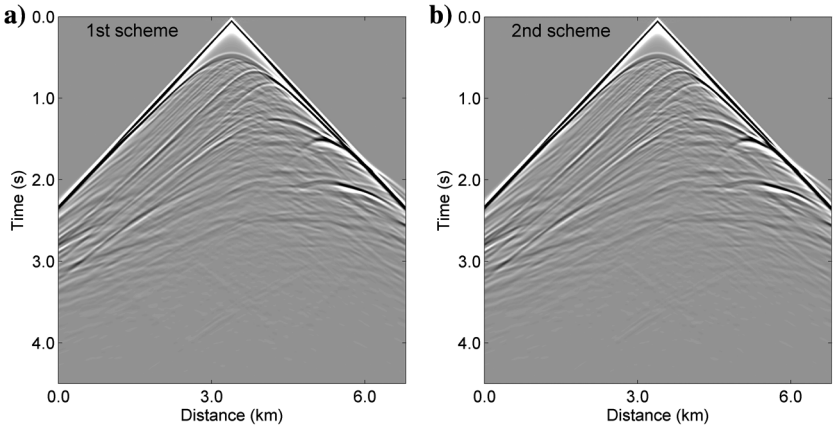

Figure 10. Seismic recordings at the surface computed by the (a) first and second scheme.

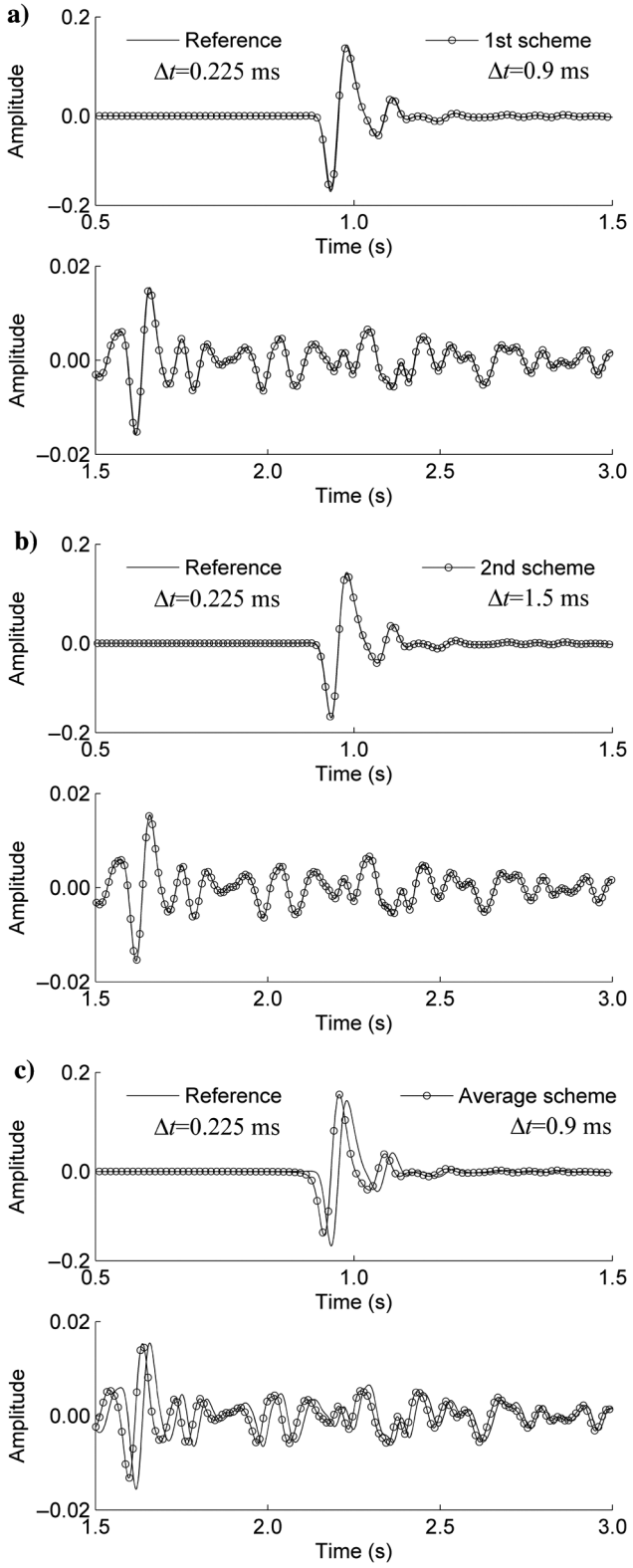

Figure 11. Trace comparison at $x = 2$ km in Figure 10, between reference and that computed by (a) the first scheme, (b) the second scheme, and (c) the Zhu and Harris (2014) averaging scheme.

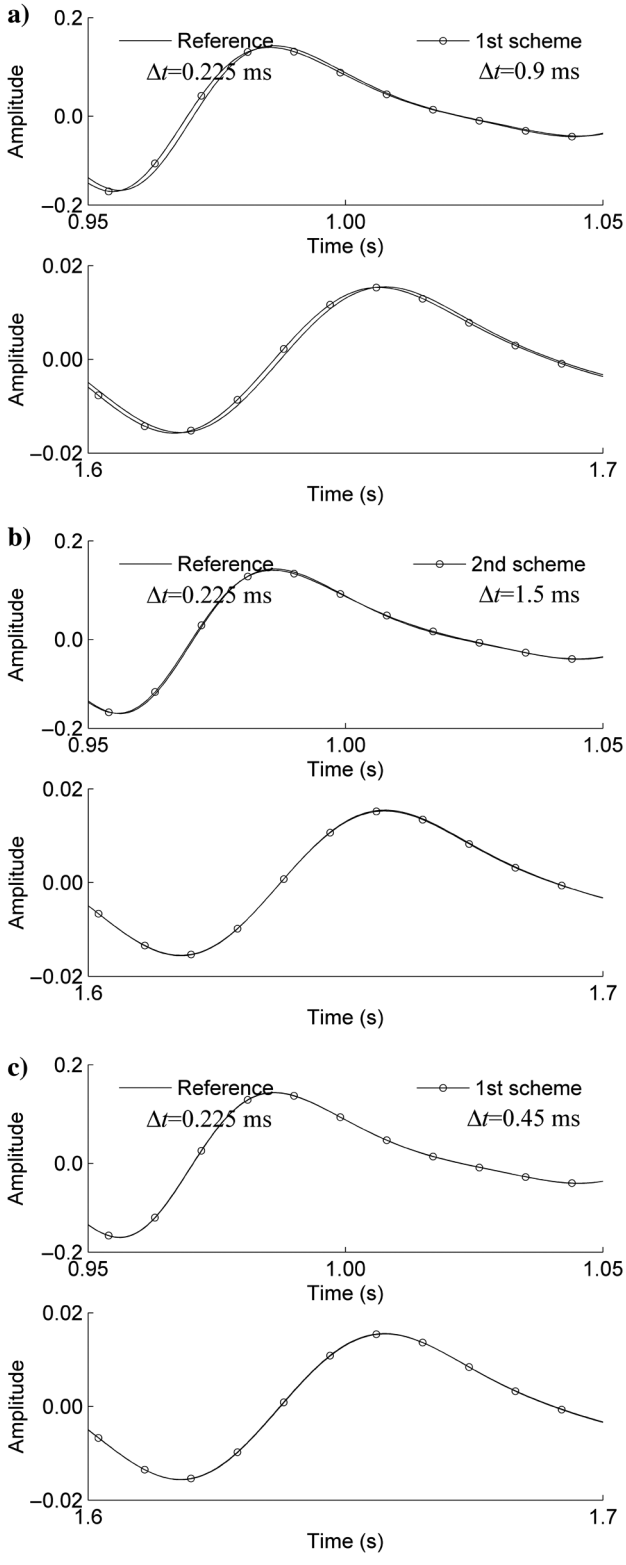

Figure 12. A closer look of waveform during 0.95–1.05 s and 1.6 –1.7 s, simulated by (a) the first scheme with $\Delta t = 0.9$ ms, (b) the second scheme with $\Delta t = 1.5$ ms, and (c) the first scheme with $\Delta t = 0.45$ ms.

To demonstrate the low-rank decomposition accuracy for the Marmousi model, we select two spatial positions to observe the decomposition error. The first spatial position is located at $(x, z) = (990, 990)$ m, where $c_o = 1849$ m/s and $Q = 54$, and the second position is located at $(x, z) = (990, 2830)$ m, where $c_o = 4500$ m/s and $Q = 383$. Figure 9 displays the exact operators at these two positions calculated by equation 28 and the low-rank decomposition errors. One can observe that compared with exact operators, the low-rank decomposition errors with the ranks of $m = n = 4$ have a small magnitude, which indicates that the ranks of $m = n = 4$ can ensure a sufficient accuracy during wave propagation.

Figure 10 displays seismic recordings at the surface computed by the first and second modeling schemes. In general, the two recordings agree with each other very well. In Figure 11, we compares the traces at $x = 2$ km, computed by our two schemes, and Zhu and Harris (2014) averaging scheme, respectively. The reference trace is computed by numerically solving equation 1 with a tiny time step of $\Delta t = 0.225$ ms. The used numerical scheme to obtain the reference is described in Appendix C. In each subplot of Figure 11, the upper panel shows the waveform during 0.5–1.5 s, and the lower panel shows the waveform during 1.5–3.0 s. Figure 11a and 11b displays good matches between the reference and the traces simulated by our two schemes. However, the trace computed by the average scheme exhibits a visible phase-shift off the reference, as displayed in Figure 11c.

For a clear comparison, we magnified the traces in Figure 11a and 11b, and redisplay them in Figure 12a and 12b, respectively. One can find a visible phase advance of the trace computed by our first scheme in Figure 12a. In contrast, the trace simulated by our second scheme fits the reference well, as shown in Figure 12b. When a two times smaller time step of $\Delta t = 0.45$ ms is used in the first scheme, the temporal dispersion decreases, and the simulated trace matches the reference very well, as shown in Figure 12c. However, when the time step is halved, the elapsed CPU time of the first scheme approximately doubles, as listed in the third row of Table 5. Therefore, to attain a comparable accuracy in this numerical test, the second scheme runs almost two times faster than the first scheme.

DISCUSSION

In this section, we discuss the feasibility of applying an empirical approximation to our wave equations 15 and 25. Taking equation 24 for example, we conduct the following empirical approximation:

$$\bar{\tau} k^{2\gamma+1} = -\frac{1}{Q} c_o^{2\gamma+1} \omega_o^{-2\gamma} k^{2\gamma+1} = -\frac{\lambda c_o}{Q} k \left(\frac{k}{k_d}\right)^{2\gamma} \rightarrow -\frac{\lambda c_o}{Q} k^{1.01}. \tag{30}$$

According to Zhu and Harris (2014), the operator $\bar{\tau} k^{2\gamma+1}$ dominates amplitude attenuation. We have further observed that the attenuation rate is mainly controlled by the coefficient of c_o/Q. For a given

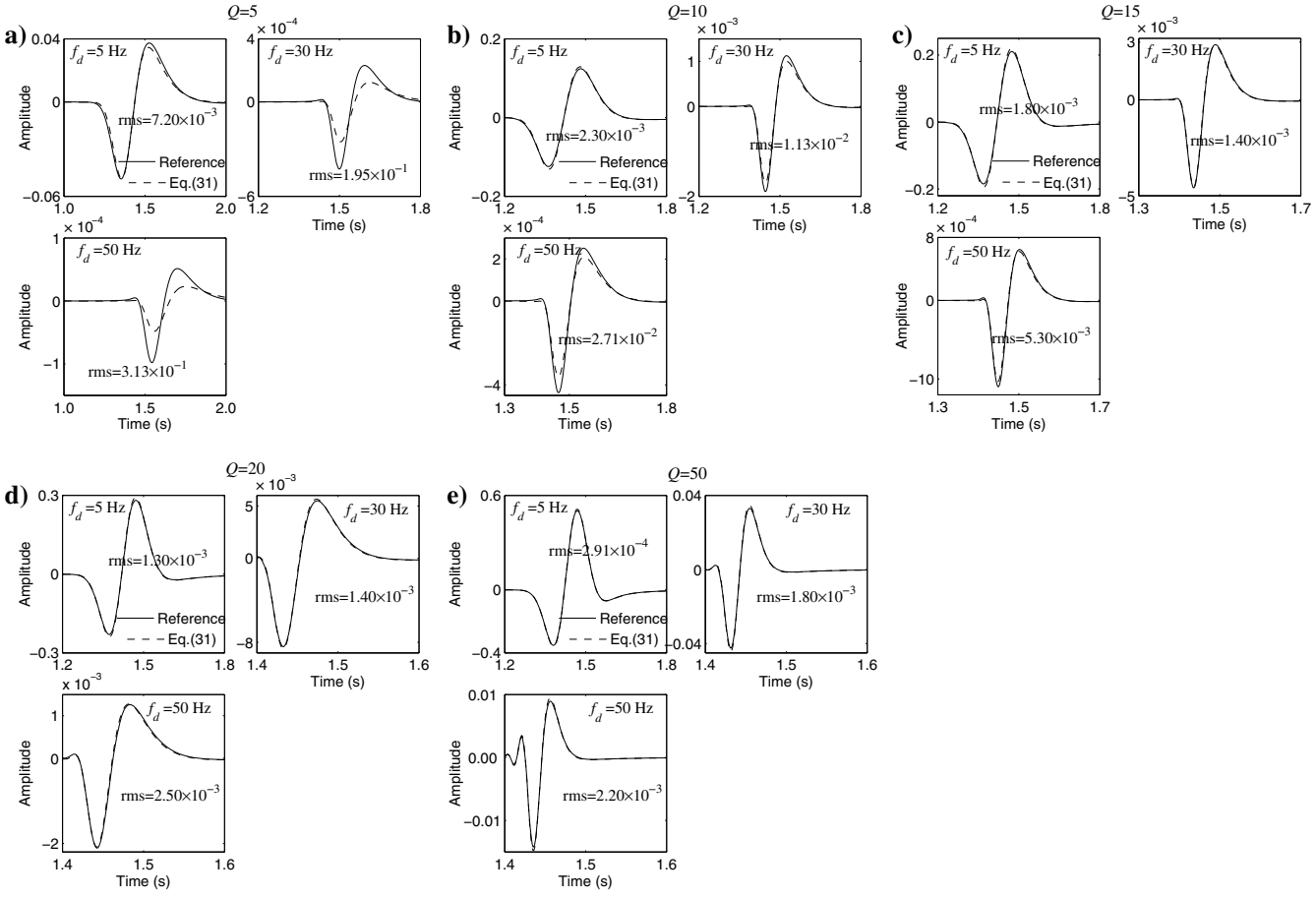

Figure 13. Comparison of numerical solutions between equations 1 (reference) and 31 for (a) $Q = 5$, (b) 10, (c) 15, (d) 20, and (e) 50.

wavenumber component, the fractional order γ only has a weak effect on the operator $k(k^{2\gamma}/k_d^{2\gamma})$, which further makes it have no dominant contribution to the attenuation rate. For that reason, we empirically conduct the approximation in equation 30. One may adopt other fractional orders of the wavenumber, e.g., 1.0, 1.02, or other values close to 1.0 in equation 30. A tiny perturbation of the fractional order would not introduce great differences to the amplitude of simulated waves.

When the empirical approximation is applied to equation 13, our wave equation 15 is simplified into

$$\frac{1}{\lambda c^2\cos(\pi\gamma)}\frac{\partial^2 p}{\partial t^2} = \left(1-\frac{2}{\varepsilon\pi Q}\right)\nabla^2 p - \frac{2}{\varepsilon\pi Q}\left(\frac{c_o}{\omega_d}\right)^{\varepsilon}(-\nabla^2)^{1+0.5\varepsilon}p - \frac{1}{Qc_o}\frac{\partial}{\partial t}(-\nabla^2)^{0.505}p. \tag{31}$$

Similarly, our wave equation 25 is simplified into

$$\frac{\partial^2 p}{\partial t^2} = \bar{\eta}^2\hat{\nabla}^2 p - \frac{\lambda c_o}{Q}\frac{\partial}{\partial t}(-\nabla^2)^{0.505}p. \tag{32}$$

Compared with equations 15 and 25, numerical simulations of equations 31 and 32 have higher computational efficiency because they contain fewer fractional Laplacians.

If one conducts a relative error analysis for the approximation in equation 30, one can find that it introduces large errors. However, the approximation indeed shows a strong robustness in numerical simulation, which ensures the accuracies of equations 31 and 32. To demonstrate the simulation accuracy, we compare numerical solutions of equation 31 with that of the original equation 1 at a distance of 5 km from the source. The numerical solution of equation 1 is regarded as a reference. The homogeneous medium with $c_o = 4000$ m/s is used again. We conduct the numerical solution comparison for $Q = 5$, 10, 15, 20, 50 in Figure 13a–13e, respectively. We adopt the Ricker wavelets with $f_d = 5$, 30, and 50 Hz as sources for each Q. Figure 13 indicates that the rms error of the numerical solutions of equation 31 generally increases with f_d, but reduces with the increase of Q. Relatively large rms errors appear when $Q = 5$, 10 with $f_d = 30$, 50 Hz, as shown in Figure 13a and 13b. However, for $Q = 15$, the rms errors become small, and the simulated waveform by equation 31 matches the reference well, especially for $f_d = 5$, 30 Hz, as displayed in Figure 13c. When Q further increases to 20 and 50, the rms error of the numerical solution of equation 31 decreases further.

One can also compare the rms errors in Figure 13 with those in Figure 2 (see the panels with $\varepsilon = 1/16$), and conclude that equation 15 has a higher accuracy than our equation 31 because the former applies a more reasonable TE approximation to approximate the fractional Laplacian dominating amplitude loss. However, Figure 13 verifies that for $Q \geq 15$ equation 31 also shows a good accuracy over long-distance propagation. Similarly, equation 32 has a good accuracy for $Q \geq 15$ as well.

To further verify the accuracies of equations 31 and 32, we repeat the numerical tests in the "Numerical examples" section by using equations 31 and 32. Figure 14 displays a similar seismogram comparison to Figure 7b. The seismogram marked by the legend of "Empirical approximation" in Figure 14 refers to the numerical solution of equation 31, and the reference is the same as that shown in

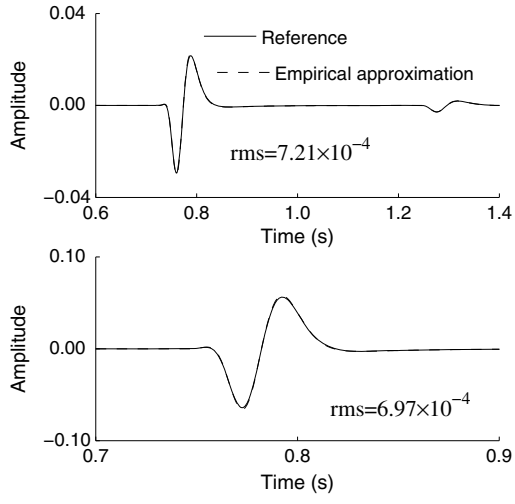

Figure 14. Similar seismograms comparison to Figure 7b. The seismograms marked by "Empirical approximation" are computed by equation 31.

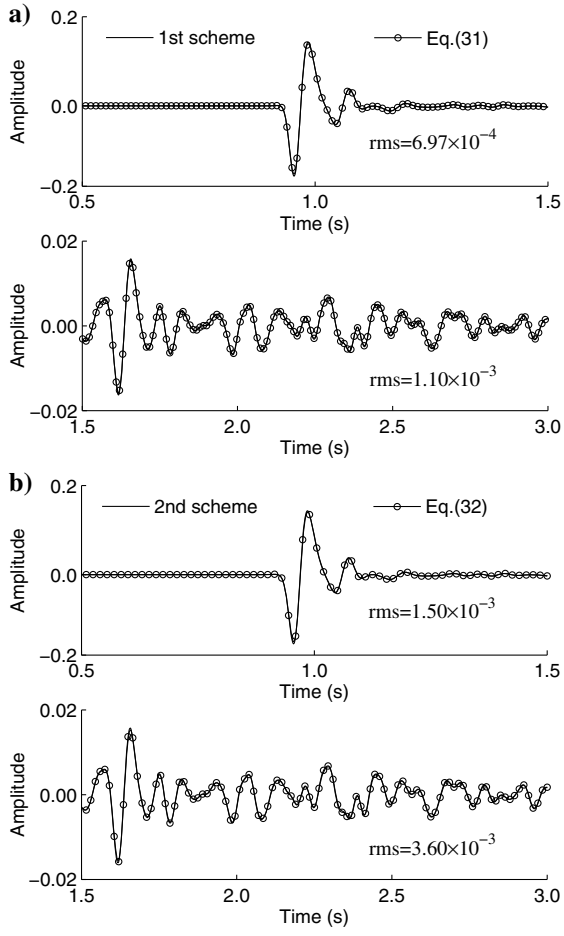

Figure 15. Simulated trace by (a) equations 15 and 31 and (b) equations 25 and 32.

Figure 7b. One can observe that the seismograms simulated by equation 31 agree with the reference very well, although the rms errors are larger than those displayed in Figure 7b.

We conduct a similar seismic trace comparison to that in Figure 11. Figure 15a shows the traces simulated by our first modeling scheme using equations 15 and 31, respectively, and Figure 15b displays the traces simulated by our second modeling scheme using equations 25 and 32, respectively. One can observe that the simulated traces in equations 15 and 31 match each other very well, and the rms error is small. Similarly, the numerical solutions of equation 32 also fit those of equation 25 very well, as displayed in Figure 15b.

CONCLUSIONS

Two efficient FFT-based modeling schemes have been developed to simulate the decoupled fractional Laplacian viscoacoustic wave equation. Both schemes can effectively handle the spatial variable-order fractional Laplacians. The first modeling scheme transforms the spatial variable-order fractional Laplacian into constant-order fractional Laplacians to facilitate numerical implementation. Numerical solution of the first modeling scheme agrees with that of the existing factional viscoacoustic wave equation very well for $Q \geq 10$. For $Q < 10$, the first modeling scheme introduces relatively large errors over long-distance propagation. The second modeling scheme is based on an analytical wave propagator, and thus it has a higher temporal accuracy. In heterogeneous media, the low-rank decomposition is applied to improve the computational efficiency of the second modeling scheme. Numerical solution of the second modeling scheme matches that of the existing factional viscoacoustic wave equation very well, even for $Q < 10$. The second modeling scheme is more efficient than the first modeling scheme because of allowing a larger time step for temporal extrapolation. To further increase computational efficiency of the two modeling schemes, an empirical approximation is applied to approximate the fractional Laplacian dominating attenuation. Numerical examples verify that the empirical approximation does not decrease the accuracies of our two modeling schemes significantly for $Q \geq 15$. The modeling schemes proposed in this paper can function as forward engines in viscoacoustic RTM and FWI. Further extending our work to variable density media and viscoelastic wave equation is possible.

ACKNOWLEDGMENTS

This work is jointly supported by the 973 Program of China (2013CB228603), National Science and Technology Program (2016ZX05010-001), National Natural Science Foundation of China (41174119), the Research of Novel Method and Technology of Geophysical Prospecting, and CNPC (2014A-3609). H. Chen appreciates Shell's Ph.D. scholarship.

APPENDIX A

ANALYTICAL SOLUTION FOR FRACTIONAL LAPLACIAN WAVE EQUATION

Equation 1 can be expressed as equation 5 in the wavenumber domain, and equation 5 can be further written as

$$\frac{d^2\tilde{p}}{dt^2} + a\frac{d\tilde{p}}{dt} + b\tilde{p} = 0, \tag{A-1}$$

where

$$a = -c^2\tau k^{2\gamma+1}, b = -c^2\eta k^{2\gamma+2}, \tag{A-2}$$

where η and τ are defined in equation 2. The analytical solution type of equation A-1 depends on the sign of the variable defined by

$$\Delta = a^2 - 4b. \tag{A-3}$$

Substitution of equation A-2 into equation A-3 leads to

$$\begin{aligned}\Delta &= c^2k^{2\gamma+2}(c^2\tau^2k^{2\gamma}+4\eta),\\ &= c^2c_o^{2\gamma}\omega_o^{-2\gamma}k^{2\gamma+2}\left\{c_o^{2\gamma}\omega_o^{-2\gamma}\cos^2\left(\frac{\pi\gamma}{2}\right)\sin^2(\pi\gamma)k^{2\gamma}-4\cos(\pi\gamma)\right\},\\ &\approx c^2c_o^{2\gamma}\omega_o^{-2\gamma}k^{2\gamma+2}\left\{c_o^{2\gamma}\omega_o^{-2\gamma}\cos^2\left(\frac{\pi\gamma}{2}\right)\sin^2(\pi\gamma)\left(\frac{\omega^{2\gamma}}{c_o^{2\gamma}}\right)-4\cos(\pi\gamma)\right\},\\ &= c^2c_o^{2\gamma}\omega_o^{-2\gamma}k^{2\gamma+2}\left\{\cos^2\left(\frac{\pi\gamma}{2}\right)\sin^2(\pi\gamma)\left(\frac{\omega^{2\gamma}}{\omega_o^{2\gamma}}\right)-4\cos(\pi\gamma)\right\}.\end{aligned} \tag{A-4}$$

Based on the CQM (Kjartansson, 1979), one has $c_p = c_o(\omega/\omega_o)^\gamma$, where c_p denotes the phase velocity. Therefore, equation A-4 can be equivalently written as

$$\begin{aligned}\Delta = {} & c^2c_o^{2\gamma}\omega_o^{-2\gamma}k^{2\gamma+2}\\ & \times\left\{\cos^2\left(\frac{\pi\gamma}{2}\right)\sin^2(\pi\gamma)\left(\frac{c_p}{c_o}\right)^2-4\cos(\pi\gamma)\right\}.\end{aligned} \tag{A-5}$$

By using $\tan(\pi\gamma) = 1/Q$, one can further express equation A-5 as

$$\begin{aligned}\Delta = {} & c^2c_o^{2\gamma}\omega_o^{-2\gamma}k^{2\gamma+2}(1+Q^2)^{-\frac{3}{2}}\\ & \times\left\{\frac{1}{2}\frac{c_p}{c_o}(\sqrt{1+Q^2}-Q)-4Q(1+Q^2)\right\}.\end{aligned} \tag{A-6}$$

Considering $c_p/c_o \approx 1$ and $\sqrt{1+Q^2}-Q \approx 0$, we have $\Delta \leq 0$ for all wavenumber components. Thus, equation A-1 has an analytical solution expressed as (Arfken et al., 2013)

$$\tilde{p}(t) = e^{\alpha t}\{A\cos(\beta t) + B\sin(\beta t)\}, \tag{A-7}$$

where A and B are two undetermined coefficients, and

$$\alpha = -\frac{a}{2}, \quad \beta = \frac{\sqrt{4b-a^2}}{2}. \tag{A-8}$$

Substitution of equation 2 into equation A-2 and further into equation A-8 leads to equation 17.

Based on equation A-7, one has

$$\tilde{p}(t+\Delta t) = e^{\alpha(t+\Delta t)}\{A\cos(\beta t+\beta\Delta t) + B\sin(\beta t+\beta\Delta t)\}, \tag{A-9}$$

$$\tilde{p}(t-\Delta t) = e^{\alpha(t-\Delta t)}\{A\cos(\beta t-\beta\Delta t) + B\sin(\beta t-\beta\Delta t)\}. \tag{A-10}$$

By expanding the trigonometric functions, e.g.,

$$\cos(\beta t+\beta\Delta t) = \cos(\beta t)\cos(\beta\Delta t) - \sin(\beta t)\sin(\beta\Delta t), \tag{A-11}$$

and using equations A-7, A-9, and A-10 together, one can readily derive the three-step time marching formula in equation 18.

APPENDIX B

PARAMETERS EXPRESSED BY VELOCITY AND Q

To simplify the characterization parameters in equations 15 and 25, we express the following parameters by c_o and Q:

$$\gamma = \tan^{-1}(Q^{-1})/\pi \approx 1/(\pi Q), \tag{B-1}$$

$$\begin{aligned} c^2\cos(\pi\gamma) &= c_o^2\cos^2\left(\frac{\pi\gamma}{2}\right)\cos(\pi\gamma) \\ &= \frac{c_o^2}{2}\left(\frac{Q}{\sqrt{1+Q^2}} + \frac{Q^2}{1+Q^2}\right), \end{aligned} \tag{B-2}$$

$$\begin{aligned} \bar{\eta} &= \frac{1}{2}c_o^{\gamma+1}\omega_o^{-\gamma}\cos\left(\frac{\pi\gamma}{2}\right)\left\{4\cos(\pi\gamma) - \cos^2\left(\frac{\pi\gamma}{2}\right)\sin^2(\pi\gamma)\right\}^{\frac{1}{2}}, \\ &= \frac{1}{2}c_o^{\gamma+1}\omega_o^{-\gamma} \\ &\times\left\{2\left(1+\frac{Q}{\sqrt{1+Q^2}}\right)\left[\frac{Q}{\sqrt{1+Q^2}} - \frac{1}{8}\left(1+\frac{Q}{\sqrt{1+Q^2}}\right)\frac{1}{1+Q^2}\right]\right\}^{\frac{1}{2}}, \end{aligned} \tag{B-3}$$

$$\begin{aligned} \bar{\tau} &= -c_o^{2\gamma+1}\omega_o^{-2\gamma}\cos^2\left(\frac{\pi\gamma}{2}\right)\sin(\pi\gamma) \\ &= -\frac{1}{2}c_o^{2\gamma+1}\omega_o^{-2\gamma}\left(1+\frac{Q}{\sqrt{1+Q^2}}\right)\frac{1}{\sqrt{1+Q^2}}, \\ &\approx -\frac{1}{2}c_o^{2\gamma+1}\omega_o^{-2\gamma}\left(1+\frac{Q}{\sqrt{1+Q^2}}\right)\frac{1}{Q} \\ &\approx -\frac{1}{Q}c_o^{2\gamma+1}\omega_o^{-2\gamma}. \end{aligned} \tag{B-4}$$

APPENDIX C

NUMERICAL SCHEME TO CALCULATE A REFERENCE WAVEFIELD IN HETEROGENEOUS MEDIA

It is unpractical to implement the pointwise FFT scheme for the Marmousi model (Figure 8) to obtain a reference seismic recording to evaluate our two modeling schemes. Here, we propose another effective numerical scheme for solving equation 1 directly, instead of solving wave equations 15 and 25.

By transforming equation 1 into the wavenumber domain, and applying FD operators to discretize the temporal derivatives, we have

$$\begin{aligned} &\frac{1}{c^2\Delta t^2}\{\tilde{p}(t+\Delta t) - 2\tilde{p}(t) + \tilde{p}(t-\Delta t)\} \\ &= \eta k^{2\gamma+2}\tilde{p}(t) + \tau k^{2\gamma+1}\frac{\tilde{p}(t) - \tilde{p}(t-\Delta t)}{\Delta t}. \end{aligned} \tag{C-1}$$

When the Q model is heterogeneous, γ varies spatially and equation C-1 contains two mixed-domain matrices

$$\mathbf{L}_1 = \mathbf{k}^{2\boldsymbol{\gamma}(\mathbf{x})+2}, \quad \mathbf{L}_2 = \mathbf{k}^{2\boldsymbol{\gamma}(\mathbf{x})+1}. \tag{C-2}$$

We incorporate the low-rank decomposition (Fomel et al., 2013) into the time marching scheme in equation C-1 to improve computational efficiency of wavefield simulation in heterogeneous media. We conduct the low-rank calculation in the same way as expressed in equation 29.

Because equation C-1 contains two mixed-domain matrices, we need to perform two times of low-rank decomposition. In addition, in equation C-1, the temporal derivatives and fractional Laplacians are approximated separately, so equation C-1 only has the first-order accuracy in time. To ensure a high accuracy, we adopt a tiny time step of $\Delta t = 0.225$ ms for avoiding temporal dispersion, and adopt relatively large ranks of $m = n = 6$ in the low-rank decomposition of the two mixed-domain matrices in equation C-2. By applying this modeling scheme, we obtain the reference trace in Figure 11.

REFERENCES

Aki, K., and P. G. Richards, 1980, Quantitative seismology: Theory and methods: W. H. Freeman.

Arfken, G. B., H. J. Weber, and F. E. Harris, 2013, Mathematical methods for physicists: A comprehensive guide: Academic Press.

Bai, J. Y., D. Yingst, R. Bloor, and J. Leveille, 2014, Viscoacoustic waveform inversion of velocity structures in the time domain: Geophysics, **79**, no. 3, R103–R119, doi: 10.1190/geo2013-0030.1.

Billette, F. J., and S. Brandsberg-Dahl, 2014, The 2004 BP velocity benchmark: 67th Annual International Conference and Exhibition, EAGE, Extended Abstracts, B305.

Blanc, É., D. Komatitsch, E. Chaljub, B. Lombard, and Z. N. Xie, 2016, Highly-accurate stability-preserving optimization of the Zener viscoelastic model, with application to wave propagation in the presence of strong attenuation: Geophysical Journal International, **205**, 414–426, doi: 10.1093/gji/ggw024.

Blanch, J. O., J. O. A. Robertsson, and W. W. Symes, 1995, Modeling of a constant Q: Methodology and algorithm for an efficient and optimally inexpensive viscoelastic technique: Geophysics, **60**, 176–184, doi: 10.1190/1.1443744.

Carcione, J. M., 2010, A generalization of the Fourier pseudospectral method: Geophysics, **75**, no. 6, A53–A56, doi: 10.1190/1.3509472.

Carcione, J. M., D. Kosloff, and R. Kosloff, 1988a, Wave propagation simulation in a linear viscoacoustic medium: Geophysical Journal of the Royal Astronomical Society, **93**, 393–401, doi: 10.1111/j.1365-246X.1988.tb02010.x.

Carcione, J. M., D. Kosloff, and R. Kosloff, 1988b, Wave propagation simulation in a linear viscoelastic medium: Geophysical Journal of the Royal Astronomical Society, **95**, 597–611, doi: 10.1111/j.1365-246X.1988.tb06706.x.

Carcione, J. M., F. Cavallini, F. Mainardi, and A. Hanyga, 2002, Time-domain seismic modeling of constant-Q wave propagation using fractional derivatives: Pure and Applied Geophysics, **159**, 1719–1736, doi: 10.1007/s00024-002-8705-z.

Chai, X. T., S. X. Wang, J. X. Wei, J. N. Li, and H. J. Yin, 2016, Reflectivity inversion for attenuated seismic data: Physical modeling and field data experiments: Geophysics, **81**, no. 1, T11–T24, doi: 10.1190/geo2015-0250.1.

Chai, X. T., S. X. Wang, S. Y. Yuan, J. G. Zhao, L. Q. Sun, and X. Wei, 2014, Sparse reflectivity inversion for nonstationary seismic data: Geophysics, **79**, no. 3, V93–V105, doi: 10.1190/geo2013-0313.1.

Chen, H. M., H. Zhou, and S. Qu, 2014, Low-rank approximation for time domain viscoacoustic wave equation with spatially varying order fractional Laplacians: 84th Annual International Meeting, SEG, Expanded Abstracts, 3400–3445.

Day, S. M., and J. B. Minster, 1984, Numerical simulation of attenuated wavefields using a Padé approximation method: Geophysical Journal of the Royal Astronomical Society, **78**, 105–118, doi: 10.1111/j.1365-246X.1984.tb06474.x.

Deng, F., and G. A. McMechan, 2007, True-amplitude prestack depth migration: Geophysics, **72**, no. 3, S155–S166, doi: 10.1190/1.2714334.

Dutta, G., and G. T. Schuster, 2014, Attenuation compensation for least-squares reverse time migration using the viscoacoustic-wave equation: Geophysics, **79**, no. 6, S251–S262, doi: 10.1190/geo2013-0414.1.

Emmerich, H., and M. Korn, 1987, Incorporation of attenuation into time-domain computations of seismic wavefields: Geophysics, **52**, 1252–1264, doi: 10.1190/1.1442386.

Fomel, S., L. Ying, and X. Song, 2013, Seismic wave extrapolation using low-rank symbol approximation: Geophysical Prospecting, **61**, 526–536, doi: 10.1111/j.1365-2478.2012.01064.x.

Kjartansson, E., 1979, Constant Q-wave propagation and attenuation: Journal of Geophysical Research, **84**, 4737–4748, doi: 10.1029/JB084iB09p04737.

Kurzmann, A., A. Przebindowska, D. Köhn, and T. Bohlen, 2013, Acoustic full waveform tomography in the presence of attenuation: A sensitivity analysis: Geophysical Journal International, **195**, 985–1000, doi: 10.1093/gji/ggt305.

Li, Q. Q., H. Zhou, S. Qu, and J. Guo, 2014, A method to improve the computational efficiency for fractional Laplacian viscoacoustic wave equation: 84th Annual International Meeting, SEG, Expanded Abstracts, 3444–3448.

Li, Q. Q., H. Zhou, Q. C. Zhang, H. M. Chen, and S. B. Sheng, 2016, Efficient reverse time migration based on fractional Laplacian viscoacoustic wave equation: Geophysical Journal International, **204**, 488–504, doi: 10.1093/gji/ggv456.

Robertsson, J. O., J. O. Blanch, and W. W. Symes, 1994, Viscoelastic finite difference modeling: Geophysics, **59**, 1444–1456, doi: 10.1190/1.1443701.

Song, X. L., S. Fomel, and L. Y. Ying, 2013, Lowrank finite-differences and lowrank Fourier finite-differences for seismic wave extrapolation in the acoustic approximation: Geophysical Journal International, **193**, 960–969, doi: 10.1093/gji/ggt017.

Sun, J. Z., S. Fomel, and T. Y. Zhu, 2014, Viscoacoustic modeling and imaging using low-rank approximation: 84th Annual International Meeting, SEG, Expanded Abstracts, 3997–4002.

Sun, J. Z., S. Fomel, and T. Y. Zhu, 2015, Preconditioning least-squares RTM in viscoacoustic media by Q-compensated RTM: 85th Annual International Meeting, SEG, Expanded Abstracts, 3959–3965.

Sun, J. Z., T. Y. Zhu, and S. Fomel, 2015, Viscoacoustic modeling and imaging using low-rank approximation: Geophysics, **80**, no. 5, A103–A108, doi: 10.1190/geo2015-0083.1.

Zhang, Y., P. Zhang, and H. Zhang, 2010, Compensating for visco-acoustic effects in reverse-time migration: 80th Annual International Meeting, SEG, Expanded Abstracts, 3160–3164.

Zhu, T. Y., J. M. Carcione, and J. M. Harris, 2013, Approximating constant-Q seismic propagation in the time domain: Geophysical Prospecting, **61**, 931–940, doi: 10.1111/1365-2478.12044.

Zhu, T. Y., and J. M. Harris, 2014, Modeling acoustic wave propagation in heterogeneous attenuating media using decoupled fractional Laplacians: Geophysics, **79**, no. 3, T105–T116, doi: 10.1190/geo2013-0245.1.

Zhu, T. Y., J. M. Harris, and B. Biondi, 2014, Q-compensated reverse time migration: Geophysics, **79**, no. 3, S77–S87, doi: 10.1190/geo2013-0344.1.